Monthly Notices of the ROYAL ASTRONOMICAL SOCIETY

MNRAS **497,** 656–671 (2020) doi:10.1093/mnras/staa1829
Advance Access publication 2020 June 27

The *XMM* Cluster Survey: new evidence for the 3.5-keV feature in clusters is inconsistent with a dark matter origin

S. Bhargava,[1,2]★ P. A. Giles,[1]★ A. K. Romer,[1] T. Jeltema,[2] J. Mayers,[1] A. Bermeo,[1] M. Hilton,[3,4] R. Wilkinson,[1] C. Vergara,[1] C. A. Collins,[5] M. Manolopoulou,[6] P. J. Rooney,[1] S. Rosborough,[1,7] K. Sabirli,[1] J. P. Stott,[8] E. Swann[1,9] and P. T. P. Viana[10,11]

[1]*Department of Physics and Astronomy, University of Sussex, Falmer, Brighton BN1 9QH, UK*
[2]*Santa Cruz Institute for Particle Physics, University of California, Santa Cruz, 1156 High St, Santa Cruz, CA 95064, USA*
[3]*Astrophysics Research Centre, University of KwaZulu-Natal, Westville Campus, Durban 4041, SA*
[4]*School of Mathematics, Statistics, and Computer Science, University of KwaZulu-Natal, Westville Campus, Durban 4041, SA*
[5]*Astrophysics Research Institute, Liverpool John Moores University, Liverpool Science Park, 146 Brownlow Hill, Liverpool L3 5RF, UK*
[6]*Institute for Astronomy, University of Edinburgh, Royal Observatory, Blackford Hill, Edinburgh EH9 3HJ, UK*
[7]*Rochester Institute of Technology, 1 Lomb Memorial Dr, Rochester, NY 14623, USA*
[8]*Department of Physics, Lancaster University, Lancaster LA1 4YB, UK*
[9]*Institute of Cosmology and Gravitation, Dennis Sciama Building, Burnaby Road, Portsmouth PO1 3FX, UK*
[10]*Instituto de Astrofísica e Ciências do Espaço, Universidade do Porto, CAUP, Rua das Estrelas, P-4150-762 Porto, Portugal*
[11]*Departamento de Física e Astronomia, Faculdade de Ciências, Universidade do Porto, Rua do Campo Alegre, 687, P-4169-007 Porto, Portugal*

Accepted 2020 June 18. Received 2020 June 17; in original form 2020 May 5

ABSTRACT

There have been several reports of a detection of an unexplained excess of X-ray emission at $\simeq$3.5 keV in astrophysical systems. One interpretation of this excess is the decay of sterile neutrino dark matter. The most influential study to date analysed 73 clusters observed by the *XMM–Newton* satellite. We explore evidence for a $\simeq$3.5-keV excess in the *XMM*-PN spectra of 117 redMaPPer galaxy clusters ($0.1 < z < 0.6$). In our analysis of individual spectra, we identify three systems with an excess of flux at $\simeq$3.5 keV. In one case (XCS J0003.3+0204), this excess may result from a discrete emission line. None of these systems are the most dark matter dominated in our sample. We group the remaining 114 clusters into four temperature ($T_{\rm X}$) bins to search for an increase in $\simeq$3.5-keV flux excess with $T_{\rm X}$ – a reliable tracer of halo mass. However, we do not find evidence of a significant excess in flux at $\simeq$3.5 keV in any $T_{\rm X}$ bins. To maximize sensitivity to a potentially weak dark matter decay feature at $\simeq$3.5 keV, we jointly fit 114 clusters. Again, no significant excess is found at $\simeq$3.5 keV. We estimate the upper limit of an undetected emission line at $\simeq$3.5 keV to be 2.41×10^{-6} photons cm^{-2} s^{-1}, corresponding to a mixing angle of $\sin^2(2\theta) = 4.4 \times 10^{-11}$, lower than previous estimates from cluster studies. We conclude that a flux excess at $\simeq$3.5 keV is not a ubiquitous feature in clusters and therefore unlikely to originate from sterile neutrino dark matter decay.

Key words: line: identification – galaxies: clusters: intracluster medium – dark matter – X-rays: galaxies: clusters.

1 INTRODUCTION

Galaxy clusters, the largest gravitationally collapsed objects in the universe, are vast assemblages of dark matter and hot gas, making them invaluable probes of both cosmology and astrophysics. The dark matter content is estimated to be roughly 85 per cent of the total cluster's mass, encompassing each member galaxy's dark matter halo in addition to a larger cluster halo. Hot, energetic gas is found between the cluster member galaxies, forming the intracluster medium (ICM). The ICM is a plasma of predominantly ionized hydrogen and helium, which emits X-ray radiation via the thermal bremsstrahlung process. The gas is additionally enriched with heavier ions, which can be detected via their emission lines in the cluster's X-ray spectrum, e.g. O, Ne, Mg, Si, S, Ar, Ca, Fe, and Ni (see Böhringer & Werner 2010, for a review). The spectral properties of clusters have been studied for several decades, so it came as a surprise when a previously unknown feature at $\simeq$3.5 keV was reported from an analysis of stacked and individual *XMM–Newton* spectra of 73 galaxy clusters (Bulbul et al. 2014, hereafter B14, $0.01 < z < 0.35$).

One interpretation of the feature found by B14 (and in subsequent analyses, see below) is the decay of dark matter in the form of a resonantly produced 'sterile' neutrino with mass $m_{\rm s} \simeq 7.1$ keV (Abazajian, Fuller & Patel 2001). Such a particle would have an associated decay mode that results in the two-body state of an active neutrino and a photon with an energy $E = m_{\rm s}/2$ (Pal & Wolfenstein 1982). Based on the Tremaine–Gunn bound (Tremaine & Gunn 1979), sterile neutrino dark matter is expected to be in the keV mass range, with $m_{\rm s} \geq 400$ eV and a lifetime of $\tau_{\rm s} \geq 10^{24}$ s (Boyarsky, Ruchayskiy & Shaposhnikov 2009). While

★ E-mail: s.bhargava@sussex.ac.uk (SB); p.a.giles@sussex.ac.uk (PAG)

the sterile neutrino hypothesis has attracted a lot of attention in the literature, alternative explanations for the ≃3.5-keV excess have been proposed. These include an interaction of axion-like particles (ALPs) with photons (e.g. Berg et al. 2017); elemental plasma transitions whose precise energy is not resolvable by current X-ray telescopes (Jeltema & Profumo 2015); and charge exchange processes due to sulphur ions (e.g. Gu et al. 2015; Shah et al. 2016).

In Bulbul et al. (2016), the B14 team followed up their original study with an analysis of stacked *Suzaku* spectra of 47 clusters ($0.01 < z < 0.45$). From the *Suzaku* data, they reported another detection of a ≃3.5-keV feature, albeit at lower significance. There have also been reports of a ≃3.5-keV excess in the spectra of individual galaxy clusters. The B14 study included an analysis of the Perseus cluster ($z \simeq 0.02$), in which a feature with an anomalously high flux (compared to stacked clusters) was detected. They suggested that contamination from the Ar XVII dielectronic recombination line at 3.62 keV was likely responsible for this anomalously high value. Another study by Urban et al. (2015) using *Suzaku* observations similarly found evidence of a ≃3.5-keV excess in both the core and the outskirts of the Perseus cluster. However, Urban et al. (2015) concluded that the flux ratio between the core and the outskirts was incompatible with a dark matter interpretation. Moreover, recent high-resolution observations of the Perseus cluster by the *Hitomi* satellite failed to find any evidence for a discrete emission line at ≃3.5 keV (e.g. Aharonian et al. 2017; Tamura et al. 2019). The Urban et al. (2015) study also included individual analyses of three other nearby X-ray bright clusters (Coma, Virgo and Ophiuchus) but found no evidence of an excess in their respective spectra. Two of these clusters – Coma and Ophiuchus – were also stacked in B14 along with Centaurus, yielding no evidence of a line.

In addition to the cluster studies outlined above, there have been several searches for a flux excess at ≃3.5 keV in the X-ray spectra of other types of astrophysical systems. For example, Boyarsky et al. (2014) reported a detection of a feature consistent with a ≃3.5-keV emission line in the spectrum of the Andromeda galaxy (M31), although a subsequent analysis found its observed spectrum to be consistent with no excess at ≃3.5 keV (Jeltema & Profumo 2015). Boyarsky et al. (2018) reported a detection of a feature consistent with a ≃3.5-keV emission line in observations of the Galactic Centre (GC). However, Jeltema & Profumo (2015) had previously interpreted the signal in this region of the GC spectrum as the result of plasma emission lines. Furthermore, an analysis of *Chandra* observations of the GC reported no detection of a ≃3.5-keV feature (Riemer-Sørensen 2016). Other searches for a ≃3.5-keV feature have analysed the spectra of the Galactic bulge (Hofmann & Wegg 2019); individual galaxies (Anderson, Churazov & Bregman 2015; Jeltema & Profumo 2016; Ruchayskiy et al. 2016); galaxy stacks (Malyshev, Neronov & Eckert 2014); and X-ray blank sky observations of the Milky Way (Dessert, Rodd & Safdi 2020).

In this work, we revisit the seminal work of B14 by searching for a ≃3.5-keV flux excess in *XMM–Newton* cluster spectra. Our cluster sample is larger than its precursor, 117 clusters compared to 73 studied in B14, allowing us to examine the detectability of a potential dark matter decay line at ≃3.5 keV as a function of X-ray temperature ($T_{\rm X}$) and, hence, dark matter halo mass. If a ≃3.5-keV line is detected, and its flux increases with $T_{\rm X}$, then that would lend weight to a dark matter interpretation. However, if the flux weakens with $T_{\rm X}$, then an astrophysical origin would be more likely, since

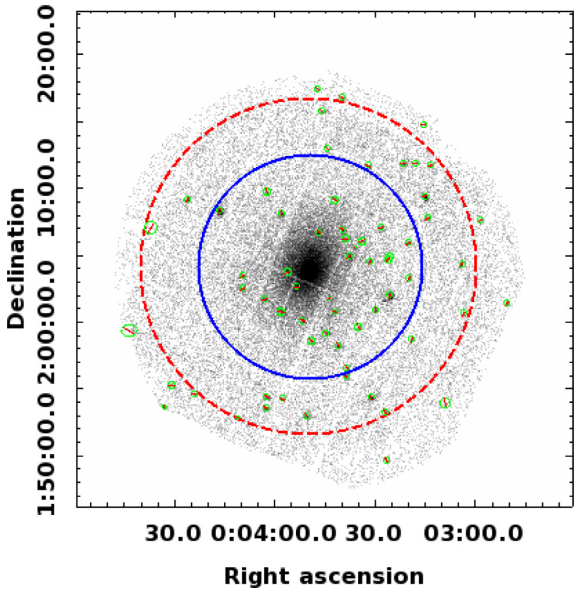

Figure 1. *XMM–Newton* image of XCS J0003.3+0204 in the 0.5–2.0 keV band. The source region is defined by the blue circle. The red dashed-circle defines the background region. Point sources are circled in green and excluded from the spectrum. The cluster image is a composite of PN and MOS observations (ObsID: 0201900101) with an associated redshift from the SDSSRM catalogue of $z_{\rm phot}^{\rm RM} = 0.11$.

prominent emission lines in the 3–4 keV region, e.g. K XVII, Ar XVII, and K XIX, weaken with plasma temperature [see figs 4 and 8 in B14 and Urban et al. (2015), respectively].

In Section 2, we describe the sample selection. In Section 3, we describe the method used to test for the presence of a ≃3.5-keV flux excess. In Section 4, we present our results. Validation checks and implications of our results are detailed in Section 5. We state our conclusions in Section 6. Throughout the paper, the parameters R_{500} and M_{500} are calculated with respect to the critical density ($\rho_{\rm c}$) at the measured cluster redshift. We assume a flat ΛCDM cosmology with $H_0 = 70$ km s^{-1} Mpc^{-1}, $\Omega_M = 0.3$, and $\Omega_\Lambda = 0.7$. Unless otherwise stated, we use the 68 per cent (1σ) confidence level for all quoted errors in this analysis.

2 THE CLUSTER SAMPLE

For this study, we use a subset of clusters drawn from a new sample of 482 clusters presented in a companion paper (Giles et al. in preparation, G20 hereafter). The G20 sample was developed by crossmatching the redMaPPer (hereafter RM) SDSS DR8 cluster catalogue (SDSSRM, Rykoff et al. 2014) with the public *XMM–Newton* data archive, where the X-ray data were processed as part of the *XMM* Cluster Survey (XCS, Romer et al. 2001).

Of the 482 clusters in the G20 sample, 346 have reliable X-ray temperature measurements (i.e. $\Delta T_{\rm X}/T_{\rm X} < 0.25$) in the redshift range $0.1 < z_{\rm phot}^{\rm RM} < 0.6$. The temperatures in G20 are measured from all available *XMM* data for a given cluster, i.e. from the three cameras on board *XMM* – PN, MOS1, and MOS2 – and all available observations if the cluster has been exposed multiple times. The cluster spectra are extracted in the 0.3–7.9 keV energy band using circular source apertures with a radius of R_{500} and annular background regions spanning $1.05R_{500}$ to $1.5R_{500}$ (see Fig. 1 for an example). The R_{500}

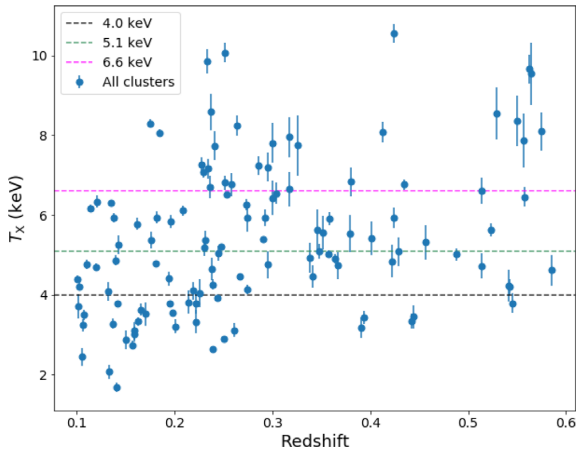

Figure 2. The X-ray temperature and redshift distributions of the 117 galaxy clusters used in this study. The dashed lines indicate the boundaries used to define each of the four temperature bins (see Table 1).

values are estimated following an iterative method using the $R_{500} - T_X$ scaling relation from Arnaud, Pointecouteau & Pratt (2005). During the spectral fitting, three of the five parameters are frozen: the redshift at the value given in the SDSSRM catalogue (a photometric estimate with $|\Delta z|/(1+z) \simeq 0.006$ where $\Delta z = z_{\rm phot}^{\rm RM} - z_{\rm spec}$), the metal abundance at $Z_\odot = 0.3$ (a value typical for X-ray clusters, see Kravtsov & Borgani 2012), and hydrogen column density, $n_{\rm H}$, at the value obtained from the HI4PI survey (Ben Bekhti et al. 2016). The remaining two parameters, T_X and normalization, are left free. More detail about the crossmatching process between SDSSRM and XCS, X-ray spectral analysis, and quality control methods can be found in G20.

For the purposes of the current study, we require high-fidelity X-ray spectra. Therefore, rather than using all 346 clusters, we apply additional quality controls, detailed as follows. First, we re-derive T_X and ΔT_X values using only data from the PN camera and, if multiple observations are available, only from the longest cleaned exposure of a given cluster. We compute the cumulative cleaned exposure time from each PN observation in our sample, obtaining a total of 2.7 Ms of good exposure.[1] We also calculate associated 0.3–7.9 keV PN-only signal-to-noise ratios. After applying an upper limit of $\Delta T_X/T_X|^{\rm PN} = 0.1$, and a lower limit signal-to-noise ratio of SNR = 25, 117 clusters remain. Relevant properties of the 117 clusters are presented in Table A1, and Fig. 2 shows the sample distribution of X-ray temperature and RM determined redshifts. Only 13 of these clusters are found to be in common with the B14 analysis (these are indicated in Appendix A1).

3 METHODOLOGY

3.1 Blueshifting to the rest frame

Before carrying out spectral fits (described in Section 3.2), the spectra are blueshifted (i.e. so that $z_{\rm effective} = 0$). This is not strictly necessary when examining individual clusters but is required when performing joint fits. For joint fits, the blueshifting process has the additional advantage of 'smearing out' any redshift-independent instrumental artefacts that could be mistaken for astrophysical emission lines.

The format of a source spectrum measured by the detector is a list of photon counts as a function of channel number. The associated cluster response matrix file (`RMF`) and ancillary response file (`ARF`) contain the energy ranges corresponding to the source spectrum channels. Each cluster spectrum is blueshifted by rescaling the upper and lower energy bounds for each photon channel by a factor of $1 + z$. This shifts the number of photons associated with each energy according to the observed redshift of the cluster. Because the source and background spectra both rely on the `ARF` and the `RMF`, modifications to both spectra are required to ensure consistency. We present a validation check of the blueshifting technique in Section 5.2.1. We note that our approach to blueshifting is the same as that used in B14.

3.2 Spectral fitting

We have carried out three separate but related tests on the cluster spectra: the first is on the 117 clusters separately (Section 4.1) to determine any outliers with excess flux at $\simeq$3.5 keV. The second is a joint fit to clusters binned into four different temperature bins (Section 4.2, with and without outliers). The third is a joint fit to the whole sample (minus the outliers, see Section 4.3). Each test is progressively more sensitive to the existence of a dark matter decay spectral feature. The second test also allows us to search for a potential mass dependence of a $\simeq$3.5-keV feature, because T_X is a robust tracer of the underlying dark matter mass. Hence, evidence of an increase in a $\simeq$3.5-keV flux excess with T_X would give firm support to the dark matter interpretation (and vice versa). For each test, we carry out a fit to a fiducial model ('model A': `tbabs × apec`) and then compare the goodness of fit to a model that includes an addition emission line component ('model B': `tbabs × (apec + weight × Gaussian)`) to mimic a dark matter decay feature. The fitting is performed using XSPEC version 12.10.1F (Arnaud 1996), APEC version 3.0.9, and solar abundances based on Anders & Grevesse (1989), using the XSPEC `cstat` statistic.

There are five parameters in model A. Three are frozen during the fit: the $n_{\rm H}$ value, the X-ray temperature (at the $T_X^{\rm PN}$ value, see Section 2), and the redshift (at $z_{\rm effective} = 0$). Two are left free: the APEC normalization, and the metal abundance. During joint fits, the abundance is 'tied' across all the spectra being examined. This results in an average abundance per fit (see column 5 in Table 1). For both individual and joint fits, the normalization of the electron plasma density is fitted separately to each cluster.

There are nine parameters in model B. Five of these are shared with model A and treated in the same way during the fit. The remaining four parameters are associated with the Gaussian component: the central energy, line width, normalization, and a constant weighting factor ($0 < weight < 1$). The central energy is frozen at a value iterated between 3 and 5 keV in intervals of 25 eV, i.e. 80 separate fits to model B are run for a given analysis. The line width is fixed at zero to mimic the narrowest possible line emission allowed by the energy resolution of the detector, which is in turn defined by the `ARF` matrix associated with the respective cluster spectrum. The normalization is a free parameter but, like the metal abundance, is fitted jointly or 'tied', generating an average fitted value per bin. The weighting factor is an input to the model and frozen

[1] Compared to 2.0 Ms of PN data in B14.

Table 1. Properties of the cluster sample according to binned X-ray temperature.

Bin number	T_X bin (keV)	No. of clusters	T_X average (keV)	M_{DM}^{proj} average ($10^{14}\,M_\odot$)	Fitted abundance $Z_\odot$	SNR average 0.3–7.9 keV	SNR average 3.0–4.0 keV
1	≤4	30	3.24	1.88	0.24	89.6	14.7
2	4–5.1	29	4.60	3.26	0.34	118.9	22.8
3	5.1–6.6	28	5.82	4.92	0.20	179.0	37.1
4	≥6.6	30	7.89	8.07	0.29	163.8	36.5

Note. Column (1): bin number; column (2): temperature range of the bin; column (3): number of clusters in bin; column (4): average temperature of bin; column (5): average projected dark matter mass (M_{DM}^{proj}); column (6): fitted abundance (in units of solar metallicity); column (7): average SNR in the 0.4–7.9 keV band; and column (8): average SNR in the 3.0–4.0 keV band.

during the fit. Each cluster has a different assigned weight (see Section 3.2.2).

We define the parameter ΔC to quantify the change in the goodness of fit between the two models at a given energy E, where $3 < E < 5$ keV (see above). ΔC is the difference between the value of the Cash statistic (Cash 1979) after fitting for model A and the value after fitting for model B. A positive value of ΔC indicates that the fit is better for model B. The estimate for the 3σ threshold (i.e. the value of ΔC above which is considered a significantly better fit) is calculated based on the probability of exceeding 99 per cent significance for model B compared to model A, taking into account the fact that model B has one additional degree of freedom.

3.2.1 *Differences to the B14 method*

Our analysis differs from B14 in several ways. First, we implement the APEC plasma model using the standard approach, i.e. relying on predefined emissivities taken from ATOMDB (Foster et al. 2012) to account for emission lines. B14 alternatively define a line-free APEC plasma model with 28 Gaussian models added to account for emission lines (though some are later removed to improve convergence of their fits). Next, with respect to photoelectric absorption, we use the `tbabs` cross-sections, whereas B14 adopt the `wabs` values (see Section 5.2.4). Our methods also differ in the approach to background subtraction. We use an infield background subtraction method (see Section 2). B14 use a composite background model that accounts for contributions from the quiescent particle background, the cosmic X-ray background, solar wind charge exchange, and residual contamination from soft protons. Furthermore, we use the ΔC parameter to assess the change in the goodness of fit between models A and B (following a similar analysis undertaken by Urban et al. 2015), whereas B14 uses a χ^2 approach.

While we fit each spectrum in parallel when performing joint fits, B14 stack their data into a composite spectrum first. The advantage of our method is that it allows us to explore the influence of individual spectra on the joint fit (see Section 3.2). Moreover, in our study, we have focused on *XMM*-PN data, whereas B14 also fitted to *XMM*-MOS, as well as analysing the *Chandra*-ACIS spectra of Virgo and Perseus.

Finally, when searching for evidence of a 3.5-keV feature, the energy values in our analysis are frozen in intervals of 25 eV (e.g. 3.5, 3.525, 3.55, 3.575, 3.6) whereas B14 nominally compute a best-fitting value for their energy of an unidentified line in their stacked spectrum. However, we note that out of the 14 fits in their study, best-fitting values are computed only for the full *XMM* PN and MOS samples. Stacked spectra consisting of fewer clusters subsequently assume a fixed energy at 3.57 keV. Similarly, for the *Chandra* ACIS spectra, a best-fitting energy is computed for Perseus and subsequently frozen at 3.56 keV in the *Chandra* spectrum of Virgo.

3.2.2 *Dark matter flux and weighting*

If a flux excess (over the fiducial model A) originates from dark matter decay, then for a given cluster, we would expect the flux to increase with the projected dark matter mass in the *XMM* FOV, M_{DM}^{proj}, but to decrease with cluster redshift, z. To account for this, M_{DM}^{proj} and z dependent weights are applied during the joint spectral fits. The M_{DM}^{proj} values are defined within a radius $R_{ext} = R_{500}$, i.e. the same extraction aperture as the PN spectrum (stated in Section 2). The total masses for the clusters are estimated by applying the $M_{500} - T_X$ scaling relation described in Arnaud et al. (2005). These are then corrected for the fact that the dark matter accounts for only 85 per cent of the total mass, and the projected dark matter mass within a R_{500} cylinder is larger than that within a sphere.[2] The projected dark matter mass for each individual cluster is stated in column 4 in Table A1. The average projected dark matter mass for each temperature bin is stated in column 4 of Table 1.

For the joint fits, to account for a different dark matter contribution from each cluster, we apply a weighting to each cluster during the fits to model B. We calculate the weighting w_i from each cluster i in a given temperature bin according to

$$w_{i,DM} = \frac{M_{i,DM}^{proj}(< R_{ext})(1+z_i)}{4\pi d_{i,L}^2}, \quad (1)$$

where $d_{i,L}$ is the luminosity distance at z_i. Before the fitting to model B takes place, the individual cluster weights $w_{i,DM}$ are normalized by the largest value in the chosen bin, i.e. one cluster per bin has a $weight = 1$, while remaining clusters have $0 < weight < 1$. During the fits to individual clusters, the weighting is assigned to unity.

3.3 Estimation of sterile neutrino mixing angles

If a measured flux excess is due to dark matter decay, we can estimate a sterile neutrino mixing angle using the Gaussian line normalization taken from the fit to model B. For this, we use the B14 relation between decaying dark matter flux, F_{DM} and projected dark matter

[2]This is done following the method in Łokas & Mamon (2001), assuming a concentration parameter, $c_{500} = 3$, based on the $c_{500} - M_{500}$ scaling relation described in Vikhlinin et al. (2006).

mass,

$$\sin^2 2\theta = \frac{F_{\rm DM}}{12.76\,{\rm cm^{-2}s^{-1}}}\left(\frac{10^{14}M\odot}{M_{\rm DM}^{\rm proj}}\right) \times \left(\frac{d_L}{100\,{\rm Mpc}}\right)^2\left(\frac{1}{1+z}\right)\left(\frac{\rm keV}{m_s}\right)^4. \quad (2)$$

4 RESULTS

4.1 Fits to individual clusters

To look for evidence of a ≃3.5-keV feature in individual cluster observations, as has previously been reported from Perseus (e.g. B14, Urban et al. 2015; Franse et al. 2016), we perform a ΔC analysis on each of the 117 clusters in our sample, using the methodology described in Section 3.2. We find evidence for a $>3\sigma$ fit improvement at ≃3.5 keV in three cases: XMMXCS J000349.3+020404.8 (hereafter XCS J0003.3+0204), XMMXCS J141627.7+231523.5 (hereafter XCS J1416.7+2315), and XMMXCS J222353.0−013714.4 (hereafter XCS J2223.0–0137). The results are shown in Fig. 3. For each cluster, the top panel shows ΔC as a function of energy, and the bottom panel shows the corresponding normalization of the Gaussian line component in units of photons $\rm cm^{-2}s^{-1}$. The horizontal blue shaded area in the top panels represents the $<3\sigma$ region. The vertical green bars in both top and bottom panels span 3.50–3.60 keV, which indicates the expected energy range in which a ≃3.5-keV line would be detected assuming the appropriate spectral resolution for the instrument. All prior detections of the 3.5-keV feature have quoted a best-fitting energy firmly within this range, hereafter known as 'the region of interest'.

For XCS J0003.3+0204 (XCS J1416.7+2315), the largest fit improvement occurs at 3.55 (3.6) keV, characterized by $\Delta C = 13.4$ (9.17) and a corresponding Gaussian line flux of $1.12^{+0.31}_{-0.31} \times 10^{-5}$ ($6.14^{+2.02}_{-1.99} \times 10^{-6}$) photons $\rm cm^{-2}\ s^{-1}$. For XCS J2223.0–0137, the maximum value of ΔC falls below the region of interest, although still exceeds 3σ therein. Further discussion of XCS J1416.7+2315, XCS J0003.3+0204, and XCS J2223.0−0137 can be found in Sections 5.1.2, 5.1.1, and 5.1.3, respectively.

The sterile neutrino mixing angle estimates for XCS J0003.3+0204 and XCS J1416.7+2315 are given in Table 2. We do not provide this information for XCS J2223.0–0137 because, from Fig. 3, the shape of the flux excess found in this cluster is unlikely to indicate the presence of a discrete emission feature (see Section 5.1.3). We note that the estimated $\sin^2 2\theta$ values (of order $\times 10^{-9}$) are significantly larger than those measured by B14, based on the PN-only result for their full sample as well as individual clusters, i.e $4.3^{+1.2}_{-1.0}10^{-11} < \sin^2 2\theta < 1.9 \times 10^{-10}$ (as quoted in table 5 of B14).

4.2 Joint fits to sub-samples binned by temperature

To test for a potential temperature dependence of the strength of a ≃3.5-keV flux excess, the 117 clusters in the sample are subdivided into four temperature bins: ≤4 keV, 4–5.1 keV, 5.1–6.6 keV, and ≥6.6 keV, containing 30, 29, 28, and 30 clusters, respectively. For simplicity, hereafter, we refer to these temperature bins as bin 1 (≤4 keV), bin 2 (4–5.1 keV), bin 3 (5.1–6.6 keV), and bin 4 (≥6.6 keV). Properties of the bins, averaged according to the number of clusters, can be found in Table 1. In Fig. 4, we present the results of the ΔC analysis of each the four temperature bins, after removing the three cases shown in Fig. 3.

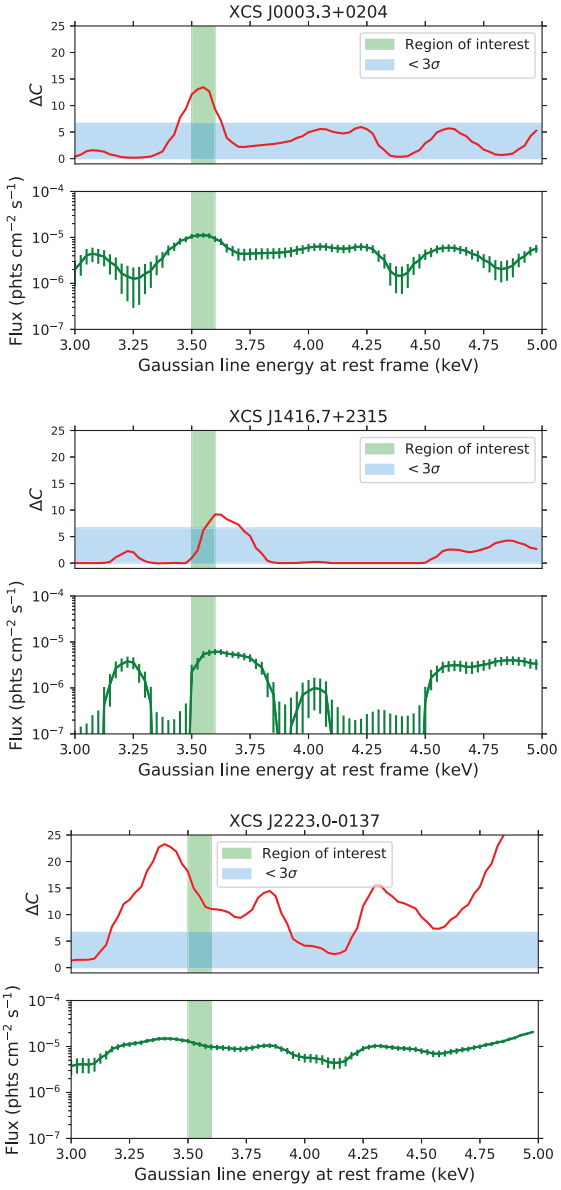

Figure 3. Top panels (red line): The change in fit statistic (ΔC) between model A and model B (see Sect 3.2) as a function of energy in the range 3–5 keV. Bottom panels (green line): Fitted normalization of the Gaussian line and corresponding errors. The value of ΔC determines the extent to which model B is a better fit to the data than model A. In each plot, the green shaded region encloses the 3.5–3.6 kev range (where a potential DM signal is expected), defined as the 'region of interest'. The light blue shaded region determines a $<3\sigma$ detection (see Section 4 for definition). The top, middle, and bottom plots refer to the clusters XCS J0003.3+0204, XCS J1416.7+2315, and XCS J2223.0−0137, respectively.

No significant fit improvement is found in any bin in the region of interest, i.e. the range defined by the vertical green bar. We note that within the four bins, there are other ranges of ΔC values that exceed a $3\,\sigma$ improvement of model B over model A. These regions correspond to energies where there are known astrophysical lines (e.g. Ar XVII complex with the strongest line at 3.32 keV, Ca XIX at 3.86 keV & 3.90 keV, Ca XX at 4.1 keV, and Ca XIX at 4.58 keV). Two prominent instrumental lines are also present; the Ti Kα at 4.51 keV, and Ti Kβ at 4.93 keV (see Jeltema & Profumo 2016). Even though the aforementioned plasma lines are

Table 2. Measured properties of the 3.5-keV excess, under the interpretation that it is due to a dark matter decay line.

Sample	Line energy (E) (keV)	ΔC	Flux (10^{-6} photons cm^{-2} s^{-1})	$M_{\rm DM}^{\rm proj}/d_L^2$ ($10^{10}\,M_\odot$ Mpc^{-2})	Mixing angle ($\sin^2 2\theta$)
XCS J0003.3+0204	3.55	13.4	$11.2^{+0.31}_{-0.31}$	0.14	$2.36^{+0.65}_{-0.65}\times10^{-9}$
XCS J1416.7+2315	3.6	9.17	$6.14^{+1.99}_{-2.02}$	0.05	$3.78^{+1.24}_{-1.23}\times10^{-9}$
Bin 2 (all 29 clusters)	3.5	11.8	$4.17^{+1.22}_{-1.22}$	0.65	$1.97^{+0.58}_{-0.58}\times10^{-10}$
114 clusters	–	–	2.41	1.65	4.4×10^{-11}

included in the latest version of the APEC model, APEC does not always correctly predict their relative fluxes as a function of plasma temperature and metal abundance (see e.g. Aharonian et al. 2018); hence, fit improvements at the location of known emission lines are not unexpected. Analysis of the Perseus core in Urban et al. (2015) has suggested underestimates of the abundances of elements including Ca XIX and Ti XXII (unresolved lines at 4.97 keV and 4.98 keV), the latter of which is responsible for a high ΔC value at $\simeq$4.9 keV in each bin (Fig. 4).

For completeness, we repeat the joint analysis of bins 1 and 2 with the clusters featured in Fig. 3 included (see Fig. 5). In Fig. 5 (b), when XCS J2223.0–0137 and XCS J0003.3+0204 are included in bin 2, there is now a $>3\sigma$ fit improvement within the region of interest. The maximal fit improvement is found when the central line energy is frozen at $E = 3.50$ keV, characterized by a $\Delta C = 11.8$ and corresponding Gaussian line flux of $4.17^{+1.22}_{-1.22}\times10^{-6}$ photons cm^{-2} s^{-1}, corresponding to a mixing angle of $1.97^{+0.58}_{-0.58}\times10^{-10}$ (see Table 2).

To further investigate the influence of individual clusters on the joint fit in each bin, a jackknifing resampling procedure is used: for a temperature bin containing N clusters, we perform N fittings in each bin containing $N-1$ clusters at five equally spaced values of the central Gaussian line energy ($3.5 < E < 3.6$ keV). The subsequent increase or decrease in the value of ΔC from each of these re-runs quantifies the dominance of $\simeq$3.5-keV photons in each individual spectrum. We find that the jackknifed iterations in bins 1, 3, and 4 do not result in a significance change in the ΔC values in the region of interest. However, in bin 2, where there is evidence for a $\simeq$3.5-keV excess in the joint fit when all 29 clusters are included, we find a significant variation in ΔC during the jackknifing (Fig. 6). This strongly implies that the detection of a $\simeq$3.5-keV excess in Fig. 5(b) is being driven by a subset of the clusters in the bin and is not a global feature.

4.3 Joint fits to the full sample

To obtain the highest possible sensitivity to a spectral feature arising from dark matter, we have carried out joint analysis using all 114 clusters without an individual $\simeq$3.5-keV excess. In this case, flux errors have been calculated only in the region of interest due to the excessive computation required for the $3 < E < 5$ keV energy range. The results are presented in Fig. 7. No significant improvement in the fit is found in the region of interest. We measure a best-fitting Gaussian flux of 1.40×10^{-10} photons cm^{-2} s^{-1} at 3.55 keV, corresponding to a mixing angle $\sin^2 2\theta = 2.5\times10^{-15}$. We note that during the fit, XSPEC failed to compute a lower limit on this value, due to the lack of flux excess in the region of interest.

To demonstrate that this lack of evidence is not a reflection of a lack of sensitivity, we have included on the lower panel of Fig. 7 an estimate of the 3σ upper limit on the flux (dashed purple line) of $F_{\rm DM} = 2.41\times10^{-6}$ photons cm^{-2} s^{-1}. The 3σ upper limit corresponds to the measured flux where the fit improvement (red line) is equivalent to the 3σ threshold for a detection (blue band). We assume negligible impact from the ARF on the flux limit across the specified energy range.

The 114 clusters in the joint fit have a weighted mass per distance squared of $1.65\times10^{10}M_\odot$ Mpc^{-2}, which corresponds to a maximum mixing angle, $\sin^2 2\theta = 4.4\times10^{-11}$. This is the most stringent mixing angle constraint obtained from our analysis – it is well below the values in Table 2 for individual clusters and bin 2 (with all 29 clusters included). Comparisons with the B14 analysis are indicated in the bottom panel of Fig. 7, where the red shaded region highlights the flux estimate obtained on the $\simeq$3.5-keV line using the stacked PN spectrum of 73 clusters. As can be seen in the plot, the upper limit of the flux as a function of energy (given by the dashed purple line) is 2σ below the preferred B14 value for the line using *XMM*-PN data of 73 clusters ($\sin^2(2\theta) = 6.7^{+2.7}_{-1.7}\times10^{-11}$). A summary of the mixing angles obtained from individual and jointly fitted clusters in this study, alongside constraints obtained from the literature (note that this is an incomplete list), is displayed in Fig. 8.

5 DISCUSSION

It is clear from Figs 4–7 that a $\simeq$3.5-keV flux excess is not a ubiquitous feature in cluster spectra. As Fig. 5(b) shows, where a flux excess exists, its strength does not increase with cluster temperature (and hence halo mass). Therefore, it seems unlikely that these and previously reported '3.5 keV line' detections have a dark matter origin. In this section, we investigate possible reasons why three clusters show an excess of emission at $\simeq$3.5 keV (Section 5.1) and test the robustness of our analysis methods to ensure that these are not somehow artificially masking a feature related to dark matter decay (Section 5.2).

5.1 Individual clusters with excess emission at $\simeq$3.5 keV

5.1.1 XCS J0003.3+0204

The cluster XCS J0003.3+0204 (better known as Abell 2700, Abell 1958), and first identified in X-rays by *ROSAT* (Ebeling et al. 2000), has an RM ID = 2789, an RM redshift of $z_{\rm phot}^{\rm RM} = 0.11$, and an RM richness of $\lambda = 38.9$. This well-studied cluster is not reported as having AGN activity or any distinct morphological or galaxy properties (e.g. Böhringer et al. 2007, 2010; Ettori et al. 2015; Holland et al. 2015; Lovisari & Reiprich 2018). The best-fitting temperature and metallicity (following method A, see Section 2) are $T_{\rm X}^{\rm PN} = 4.78^{+0.12}_{-0.12}$ keV and $Z = 0.4^{+0.04}_{-0.04}Z_\odot$, respectively. The fit values quoted here are based on *XMM*-PN observation ObsID 0201900101 (Fig. 1). This observation was made on 2004 June 24, and has a flare corrected exposure time of 19 ks. We note that the rate of flaring in the raw events file is less than 2 per cent for this

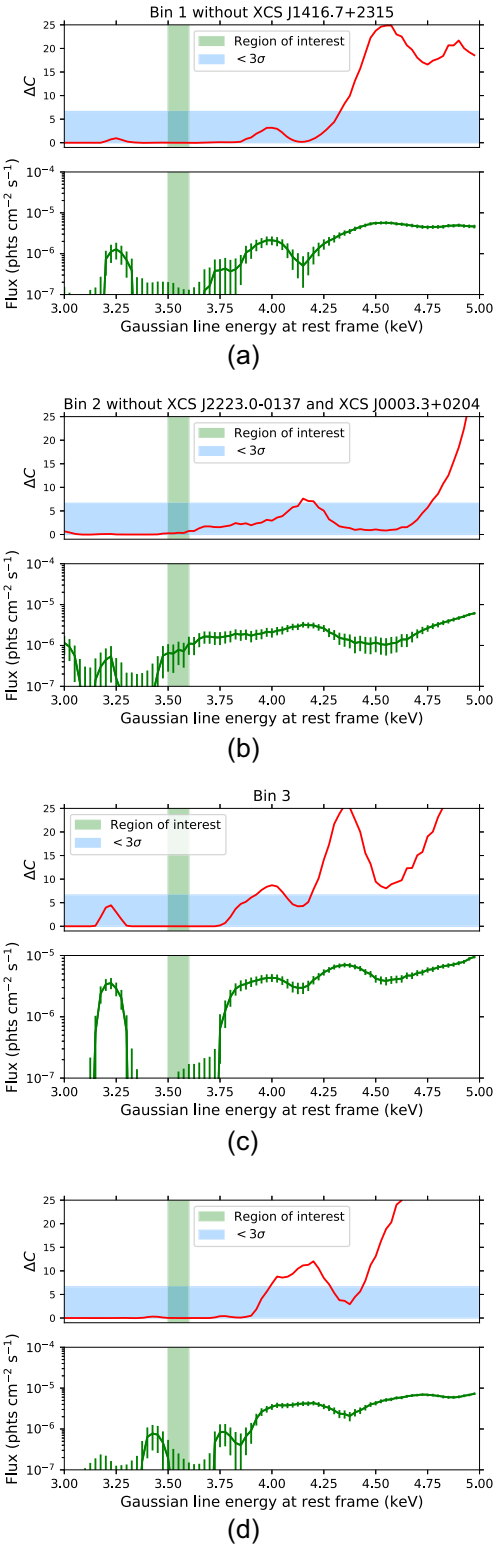

Figure 4. Similar to Fig. 3. Results from the binned subsets (see Table 1) of clusters excluding those with detected excess at ≃3.5 keV. (a): 29 clusters from bin 1 (i.e. excluding XCS J1416.7+2315). (b): 27 clusters from bin 2 (i.e. excluding XCS J0003.3+0204 and XCS J2223.0–0137). (c) 28 clusters from bin 3. (d) 31 clusters from bin 4.

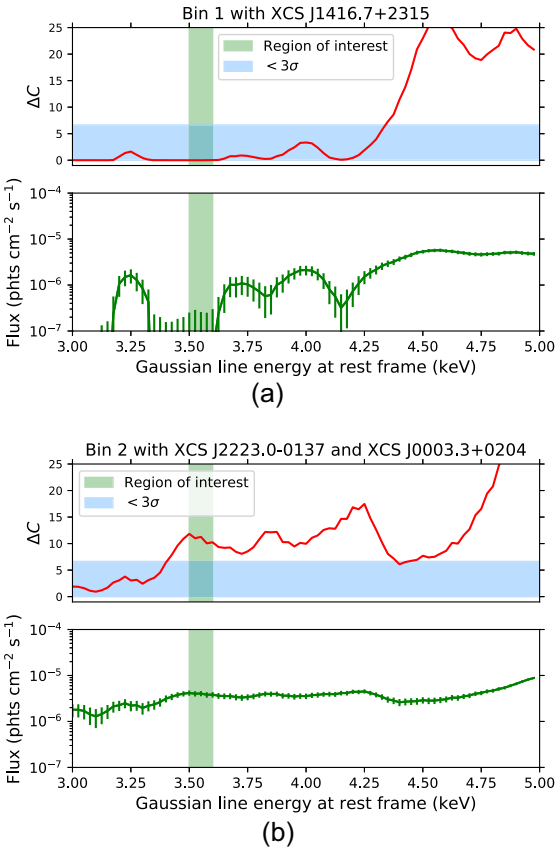

Figure 5. Similar to Fig. 4 but showing the results from the binned subsets of clusters while including those with detected excess at ≃3.5 keV (see Table 1). (a): All 30 clusters in bin 1 (i.e. including XCS J1416.7+2315). (b): All 29 clusters in bin 2 (i.e. including XCS J0003.3+0204 and XCS J2223.0–0137).

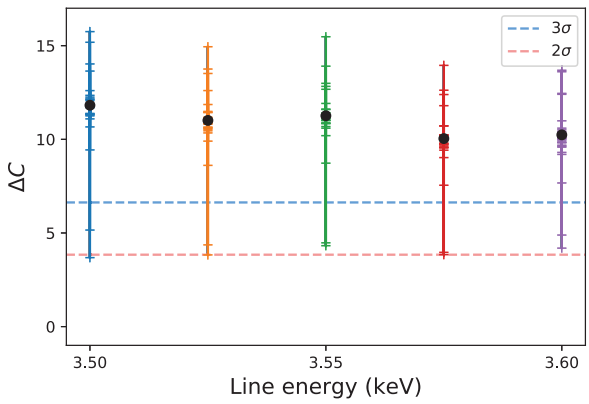

Figure 6. Variation of ΔC during a jackknife analysis performed at five energy intervals between 3.5 and 3.6 keV in bin 2 (all 29 clusters included). The black data points refer to the value of ΔC with all clusters included [i.e. the fitted value in Fig. 5(b)]. Each tick mark refers to the value of ΔC when a cluster is removed.

observation. There are no other *XMM*-PN observations available for this cluster, so we cannot investigate any possible variability in the ≃3.5-keV excess for this cluster. A comparison of the ΔC analysis between the original spectrum and one where the core region $r < 0.15R_{500}$ is excluded is shown in Fig. 9. We find that the shape of the ≃3.5-keV excess is largely insensitive to the removal of the $r <$

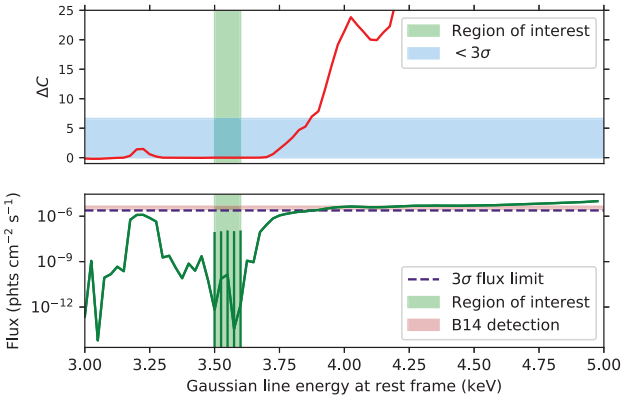

Figure 7. Similar to Fig. 4 showing the trend in ΔC using 114 clusters in the sample, minus the three clusters with known flux excess at $\simeq$3.5 keV – XCS J0003.3+0204, XCS J1416.7+2315, and XCS J2223.0–0137. In the bottom panel, the pink horizontal shaded region shows the constraints from B14 for 73 clusters (using PN data only). The dashed purple line corresponds to the 3σ flux limit defined for the sample. The fitted abundance for this analysis was $Z = 0.24 Z_{\odot}$.

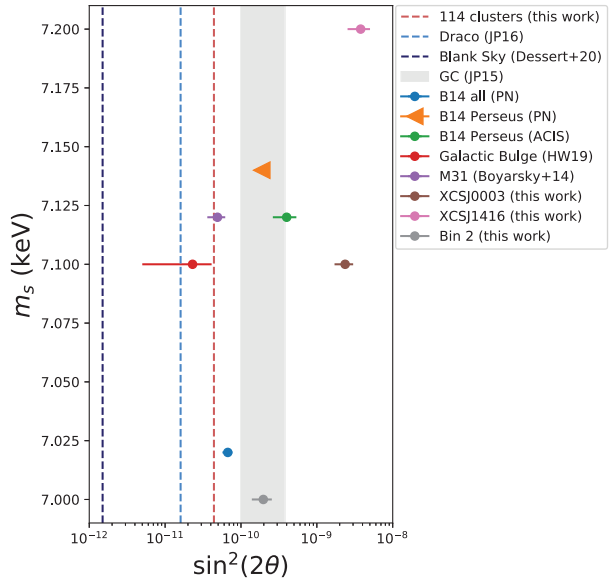

Figure 8. Comparison of the constraints on the sterile neutrino mixing angle and mass from various studies in the literature. The constraint on the mixing angle from the 114 clusters in this work is given by the pink dashed vertical line. Blue and purple dashed lines indicate upper limits from non-detections in Draco and blank sky observations, respectively. The grey shaded region highlights the range of mixing angles from the detection of a line in the Galactic Centre, depending on the choice of dark matter profile used. The remaining points correspond to detections of the line in various astrophysical systems.

$0.15R_{500}$ region. Finally, we check all available MOS data for XCS J0003.3+0204 for evidence for a 3.5-keV feature. Given the MOS camera is approximately half as sensitive as the PN, we do not expect to detect a feature at the same significance. The comparison of PN and MOS data for this cluster is shown in Fig. B1(a). We observe a feature of similar shape in the MOS2 data at a slightly higher energy ($\simeq$3.6 keV); however, there is no clear evidence of a feature within the region of interest.

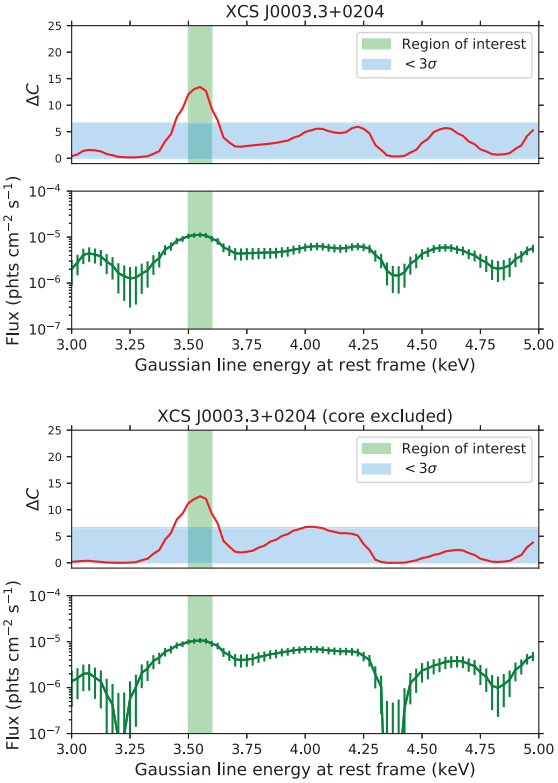

Figure 9. Plots showing the trend in ΔC (see Fig. 4 for full description) for the cluster XCS J0003.3+0204. The top plot displays the analysis using a spectrum with the core included (i.e. our standard analysis) and the bottom plot shows the trend using a spectrum with the core region excluded (see Section 5.1.1).

From the existing analysis/data, it is not possible to unambiguously explain the flux enhancement at $\simeq$3.5 keV in XCS J0003.3+0204. It is unlikely that the enhancement is related to background flare contamination, since ObsID `0201900101` is one the cleanest of the sample (of 117). The symmetrical shape of the ΔC feature, and the fact that an enhancement is visible in the spectrum (Fig. 10), supports the interpretation that this is a genuine astrophysical emission feature, either from the cluster itself or from a system along the line of sight. Despite this feature being stronger than would be expected from dark matter decay, it is not obvious that the excess is the result of a plasma transition or charge exchange process, since such a feature would also be present in other systems. One interpretation for this excess could lie in the treatment of point sources in the spectrum of XCS J0003.3+0204. As shown in Fig. 1, all point sources have been masked from the cluster observation. However, it is possible that some excess point source emission is persisting within the source region, which could be influencing the modelling of the continuum within the $\simeq$3.5-keV range (impacting the overall shape of the background/source spectrum).

This cluster is the only one of the 117 that displays a conclusive 3.5-keV feature at the $>3\sigma$ level, so it is rare. Specifically, the detection of a 3.5-keV feature in XCS J0003.3+0204 constitutes only the second ever detection of a line in a single cluster (the first being Perseus). To examine just how rare, we plan to apply our ΔC technique to the other 229 (346-117) clusters with measured $T_{\rm X}$ values in the G20 sample.

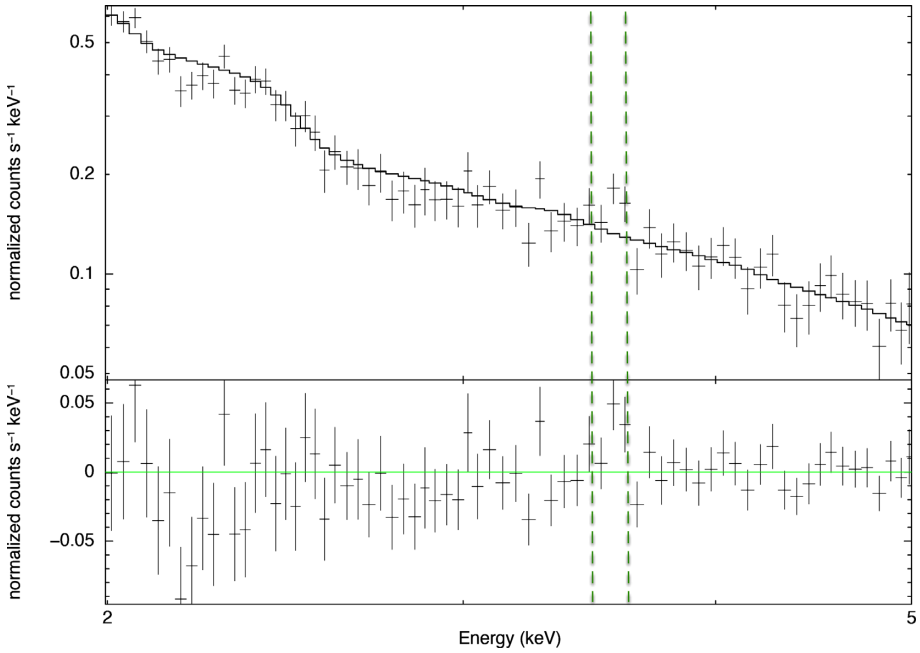

Figure 10. Spectrum of the cluster XCS J0003.3+0204 (located in ObsID `0201900101`) fitted using model A outlined in Section 3.2. The top panel shows the spectrum and fitted model across the 2–5 keV energy range. The bottom panel shows the residuals, i.e. the difference between the model and the spectrum. For visual purposes, the spectrum has been grouped such that each bin has an SNR ≥ 15. The dashed green lines enclose the 3.5–3.6 keV region of interest.

5.1.2 XCS J1416.7+2315

The cluster XCS J1416.7+2315 (first detected in X-rays by *ROSAT*, e.g. Ebeling et al. 2000), and also known as RX J1416.4+2315 (Romer et al. 2000), has an RM ID = 5527, an RM redshift of $z_{\rm phot}^{\rm RM} = 0.137$, and an RM richness of $\lambda = 31.7$. Based upon the best-fitting parameters to the *XMM*-PN spectrum using model A, described in Section 2, the cluster has a measured temperature and metallicity of $T_{\rm X}^{\rm PN} = 3.28^{+0.12}_{-0.12}$ keV and $Z = 0.17^{+0.05}_{-0.05} Z\odot$, respectively. It is noteworthy that this system has a comparatively low-metal abundance compared to the average obtained in bin 1 (see column 5 of Table 1). The $\simeq$3.5-keV excess, i.e. the region where the ΔC value is $>3\sigma$, is significantly wider than the spectral energy resolution of the *XMM*-PN detector ($\Delta E = 88$ eV).

The analysis presented in Section 4.1 and the best-fitting temperature and abundance quoted above are based on the *XMM* observation with ObsID `0722140401`. This observation was taken on 2014 January 31, and has a cleaned exposure time of 18 ks. However, this cluster has been the target of another *XMM* observation (`0722140101`). This observation was made on 2014 January 3, and has a flare corrected exposure time of 4 ks. The availability of two observations of the same cluster, made roughly a month apart, gives us the opportunity to look for time variability in the excess flux at $\simeq$3.5 keV. A comparison of the analysis between the two observations (using PN data only) is shown in Fig. 11 (top versus middle). The shorter observation (middle panel) shows a noticeably different shape of the ΔC excess at $\simeq$3.5 keV and a drop in the maximum value of ΔC in the region of interest to below 3σ. There are several possible causes for these differences. For example, they could be due to poor photon statistics in the shorter observation. Alternatively, they could be due to the differing effects of background flaring, which rises from 35 per cent of the raw events list for ObsID `0722140401` to 90 per cent for ObsID `0722140101`. Assuming the measurement of a shape and flux change is robust, then the most likely astrophysical interpretation for a time-dependent signal would be AGN variability: XCS J1416.7+2315 is described in the literature as a fossil cluster with known variable AGN activity, e.g. Miraghaei et al. (2015).

We have also investigated whether the presence of an excess at $\simeq$3.5 keV in XCS J1416.7+2315 might be associated with a cool-core. A comparison of the ΔC analysis between the original spectrum and one where the inner $0.15R_{500}$ is excluded is shown in Fig. 11 (top versus bottom). The removal of photons from the cluster core does not significantly change the shape of the ΔC excess at $\simeq$3.5 keV. The significance of the enhancement is lower after core removal but remains in excess of 3σ in the region of interest.

We repeat our analysis on this cluster using available MOS data, shown in Fig. B1(b). Yet again, owing to the differing sensitivities of the PN and MOS cameras, we do not expect to recover a significant feature in the MOS data. Interestingly, we note two narrower features in the MOS data, which align broadly with the energy of the $\simeq$3.5-keV excess in the PN spectrum of XCS J1416.7+2315.

Again, from the existing analysis/data, it is not possible to unambiguously explain the flux enhancement at $\simeq$3.5 keV in XCS J1416.7+2315. However, its broad and asymmetrical shape is not consistent with a discrete emission line origin. An additional *XMM* observation would be needed to explore the hint of time dependence seen in Fig. 11 (top versus middle). If confirmed, then AGN activity would be the most likely cause of the variability (and potentially of the $\simeq$3.5-keV flux excess). In that case, follow-up with *Chandra* would assist with resolving the central point source. Both of the *XMM* observations of this cluster (`0722140401` and `0722140101`) were taken during times of enhanced background flaring (especially `0722140101`). It would be possible to explore the impact of background flaring on the goodness of fit of model A and model B at $\simeq$3.5 keV by relaxing/tightening the criteria used to reject time periods affected by flares in these two observations.

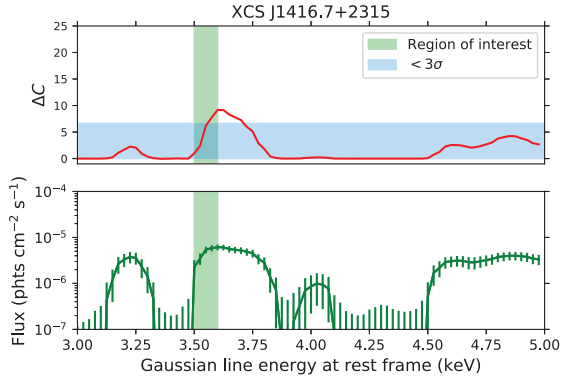

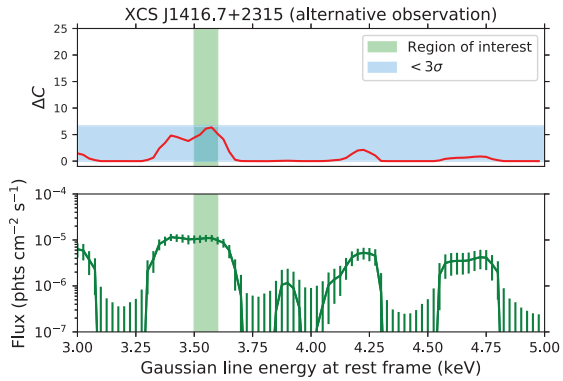

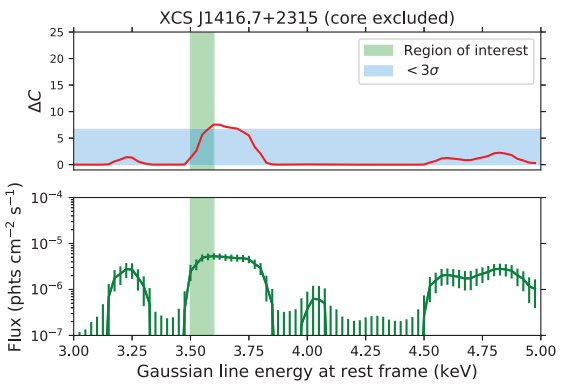

Figure 11. Plots showing the trend in ΔC (see Fig. 3 for full description) for the cluster XCS J1416.7+2315. The top plot shows the analysis using the *XMM* ObsID 0722140401 (i.e. our standard analysis), the middle plot shows the analysis performed using the *XMM* ObsID 0722140101 (see Section 5.1.2), and the bottom plot shows the analysis performed using ObsID 0722140401 with the core region excluded (see Section 5.1.2).

5.1.3 XCS J2223.0–0137

The cluster XCS J2223.0–0137 (better known as Abell 2440, Abell 1958), and first identified in X-rays by HEAO-1 (Nulsen et al. 1979), has an RM ID $= 48$, an RM redshift of $z_{\rm phot}^{\rm RM} = 0.101$, and an RM richness of $\lambda = 90.7$. The best-fitting temperature and metallicity (following method A, see Section 2) are $T_{\rm X}^{\rm PN} = 4.39^{+0.08}_{-0.10}$ keV and $Z = 0.4^{+0.04}_{-0.04} Z\odot$, respectively. The fit values quoted here are based on *XMM*-PN observation ObsID `0401920101`. This observation was made on 2006 November 18, and has a cleaned exposure time of 23 ks and a background flaring rate of 35 per cent. Due to the fact that this cluster has only one available *XMM* observation, a variability analysis cannot be performed. Furthermore, we forgo an analysis excluding the central regions of the cluster because XCS

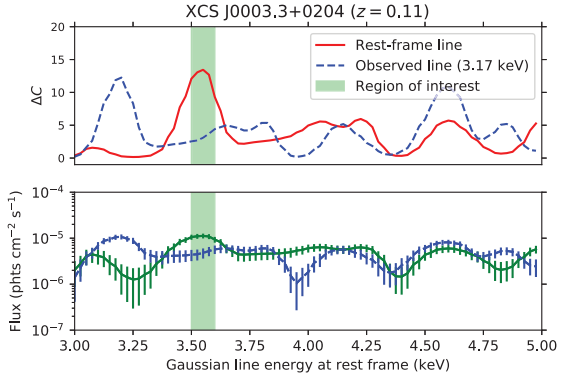

Figure 12. Plot of the change in fit statistic, ΔC (as in Fig. 4) for the cluster XCS J0003.3+0204. Our standard analysis is given by the red solid line and the blue dashed line shows the change in ΔC with the analysis performed in the observed frame, i.e. without the blueshifting step (see Section 5.2.1).

J2223.0–0137 is a complex merging system (see e.g. Mohr, Geller & Wegner 1996; Maurogordato et al. 2011) with two distinct peaks in the X-ray emission, making the exclusion of the cluster core problematic. We do, however, study the available MOS data for this cluster [Fig. B1(c)], finding no clear evidence of an excess at $\simeq$3.5 keV.

We argue that the broad ($3.25 < E < 3.85$ keV) and multipeaked shape of the $>3\sigma$ flux excess shown in Fig. 3 (bottom) is not consistent with being associated with a discrete emission line. Due to the complex cluster morphology, we forgo further discussion into the nature of the behaviour of the ΔC of XCS J2223.0–0137 in the range $3.25 < E < 3.85$ keV.

5.2 Methodology validation

In this section, we investigate the influence of various aspects of our methodology on the results presented herein: the blueshifting technique (Section 5.2.1), alternative weighting methods (Section 5.2.2), solar abundance tables (Section 5.2.3), photoelectric absorption models (Section 5.2.4), the use of photometric redshifts (Section 5.2.5), and the choice of plasma code (Section 5.2.3).

5.2.1 Blueshifting

We test our blueshifting technique using cluster XCS J0003.3+0204 (see Fig. 12). For this, we repeat the fit to model B without carrying out the blueshifting step. As expected, we find that the flux excess at $\simeq$3.5 keV now appears at the observed rather than rest-frame energy, i.e. at the expected value ($\sim$3.2 keV) for a $z_{\rm phot}^{\rm RM} = 0.11$ system (see blue dashed line in Fig. 12).

5.2.2 Flux weighting

The weighting technique described in Section 3.2.2 includes the implicit assumption that any excess flux at $\simeq$3.5 keV is due to dark matter decay. However, if the flux at that energy was instead a result of emission from the ICM, then the use of a mass-dependent weighting would be inappropriate. Therefore, we test an alternative method of weighting based only on the cluster redshift,

$$w_i' = \frac{1 + z_i}{4\pi d_{i,L}^2}, \tag{3}$$

and rerun the joint fits in each temperature bin, finding almost identical results to Fig. 4 (i.e. no $>3\sigma$ detection of a flux excess in any of the bins).

5.2.3 Solar abundance tables

Our default method uses the Anders & Grevesse solar abundance table (Anders & Grevesse 1989). We have also run the joint fits in each temperature bin, using the Lodders, Palme & Gail (2009), Asplund et al. (2009) and Grevesse & Sauval (1998) abundance tables, finding almost identical results to Fig. 4 (i.e. no $>3\sigma$ detection of a flux excess in any of the bins). Nevertheless, we note that the best-fitting metal abundance for each bin does increase slightly compared to the values in column 6 of Table 1.

5.2.4 Photoelectric absorption

Our default method uses the `tbabs` implementation of photoelectric absorption in XSPEC because the `wabs` model is now considered to be outdated (Wilms et al. 2010). However, the `wabs` model was implemented in other previous studies of the $\simeq$3.5-keV flux excess, including B14, so we have also run the joint fits in each temperature bin using `wabs` for comparison. Once again, we find almost identical results to Fig. 4 (i.e. no $>3\,\sigma$ detection of a flux excess in any of the bins).

5.2.5 Use of photometric redshift measurements

The ensemble behaviour of the $z_{\rm phot}^{\rm RM}$ is well understood. According to Rykoff et al. (2014), the scatter in the photometric redshift measurements is $\sigma_z \approx 0.006$ at $z \approx 0.1$, increasing to $\sigma_z \approx 0.020$ at $z \approx 0.5$. The median value for $|\Delta z|/(1+z)$ for the full sample is 0.006, where $\Delta z = z_{\rm phot} - z_{\rm spec}$. Therefore, the 1σ error in energy in blueshifting a 3.55-keV line to the local frame ranges from 20 eV for a cluster at $z \approx 0.1$ to 30 eV at $z \approx 0.5$, which is well below the spectral energy resolution of the PN detector ($\Delta E = 88$ eV). Therefore, it is unlikely that the use of $z_{\rm phot}^{\rm RM}$ values is the reason for a non-detection of a $>3\sigma$ detection of a $\simeq$3.5-keV flux excess in our binned analyses shown in Figs 4 and 7. For our joint fits, we conclude that the ensemble scatter in z is applicable.

However, errors in estimates of $z_{\rm phot}^{\rm RM}$ for individual clusters may influence the results discussed in Section 4.1, if they exceed the ensemble average. For the three individual clusters described in Section 5.1, the spectroscopic redshift for XCS J1416.7+2315 (Romer et al. 2001) is almost exactly the same as the RM value, $z_{\rm phot}^{\rm RM} = 0.137$. However, according to Struble & Rood (1987), XCS J0003.3+0204 (or Abell 2700) has $z_{\rm spec} = 0.0924$ based on nine cluster members, and XCS J2223.0–0137 (or Abell 2440) has $z_{\rm spec} = 0.0906$ based on 48 cluster members (compared to $z_{\rm phot}^{\rm RM} = 0.11$ and $=0.101$, respectively). Therefore, we have refitted the spectrum of XCS J0003.3+0204 and XCS J2223.0–0137 using the spectroscopic values. The results are shown in Fig. C1. We conclude that there is negligible impact from using spectroscopic redshifts, since the $\simeq$3.5-keV excess in both clusters remains within the region of interest.

5.2.6 Choice of plasma code

Searches for new emission lines are sensitive to both the temperature and metal abundance. Therefore, it is important that these properties are measured precisely to prevent erroneous detections (or non-detections) of excess flux at $\simeq$3.5 keV. As shown in detail in Mernier et al. (2020), the two codes used most in the field of X-ray cluster spectroscopy, ATOMDB and SPEXACT, do not produce consistent results for metal abundance for low-temperature plasmas. For $T_{\rm X} \leq 2$ keV, the discrepancies can be up to 20 per cent in the Fe abundance. The SPEXACT code is not implemented inside XSPEC,[3] so it is not possible to do a direct comparison here. However, only seven clusters in our sample have measured $T_{\rm X}$ values below 2 keV (and all in bin 1). Even if this issue impacts the results in plot (a) of Fig. 4, it will not impact the results shown in other three plots.

6 SUMMARY AND CONCLUSIONS

In this work, we have used a similar technique to the seminal Bulbul et al. (2014), B14, paper, in order to explore the evidence for a $\simeq$3.5-keV flux excess in the spectra of clusters of galaxies. We used individual and joint fits to *XMM*-PN spectra of 117 SDSS redMaPPer galaxy clusters ($0.1 < z < 0.6$, $1.7 < T_{\rm X} < 10.6$ keV). This is the largest study of its kind to date. By comparison, the B14 study used a sample of 73 clusters.

The analysis of the individual spectra identified three systems with an excess of flux at $\simeq$3.5 keV. This refers to an excess over the fiducial plasma model, taking into account one additional degree of freedom. None of these individual clusters are the most dark matter dominated or nearest systems in our study (see Table A1). In two of the three cases (XCS J1416.7+2315 and XCS J2223.0–0137), the flux excess, as a function of energy, is not consistent with a discrete emission feature due to the feature's broad, asymmetrical shape in both cases.

In the remaining case (XCS J0003.3+0204), the excess may result from a discrete emission line with a central energy of $E = 3.55$ keV. This feature, however, is unlikely to have a dark matter origin for two reasons. First, this is the only cluster in the sample to show such a feature, and yet there are many other observations of similar or better sensitivity in the sample. Secondly, the estimated flux ($11.2^{+0.31}_{-0.31} \times 10^{-6}$ photons cm^{-2} s^{-1}) results in significantly higher mixing angle constraints ($\sin^2(2\theta) = 2.36^{+0.65}_{-0.65} \times 10^{-9}$) than the ones presented from the stacked analysis of 73 *XMM*-PN spectra in B14. The line strength for XCS J0003.3+0204 is most comparable to the *XMM*-MOS detection for the Perseus cluster (core-included) in B14. Nevertheless, there exists an order of magnitude of difference in the derived mixing angles ($\sin^2(2\theta) \simeq 6 \times 10^{-10}$, B14).

We note that this is only the second time that a significant detection of a $\simeq$3.5-keV line-like excess has been measured in an individual cluster (the other being in Perseus). Furthermore, unlike Perseus, the strength of the 3.5-keV excess in XCS J0003.3+0204 shows almost no dependence on the removal of the core region from the spectrum. Flaring is also unlikely to be causing such an excess as we report a very low flare rate (less than 2 per cent) for this observation.

The primary motivation for our study was a search for evidence of an increase in the $\simeq$3.5-keV flux excess with $T_{\rm X}$. Such evidence would firmly support the dark matter interpretation (and vice versa if the excess weakens with $T_{\rm X}$) because $T_{\rm X}$ is a reliable tracer of the underlying halo mass. A temperature-dependent search would additionally eliminate the possibility of a plasma line masking an emission line of dark matter origin as the relevant plasma lines in the region of interest weaken with temperature (contrary to dark matter).

[3] SPEXACT is implemented in the SPEX fitting package, `www.sron.nl/astrophysics-spex`

We therefore grouped the remaining 114 clusters into four roughly equally sized T_X bins and performed joint fits in each bin. We did not find evidence of a significant excess in flux at $\simeq$3.5 keV in any of the bins. Therefore, from our study, we cannot comment on whether (if it exists at all) the $\simeq$3.5-keV flux excess gets stronger or weaker with mass. Repeating the joint fits in each bin with the inclusion of the three clusters with excess emission resulted in a significant joint detection in one bin (bin 2). However, after performing a jackknife analysis on the clusters in this bin, it is found that the joint detection is dependent on the $\simeq$3.5-keV flux excess in two individual clusters (XCS J0003.3+0204 and XCS J2223.0–0137).

We maximized sensitivity to a potential weak dark matter decay feature at $\simeq$3.5 keV by performing a joint fit across all 114 clusters. Again, no significant excess was found at $\simeq$3.5 keV. A best-fitting Gaussian flux of 1.40×10^{-10} photons cm^{-2} s^{-1} was measured at 3.55 keV, corresponding to a mixing angle $\sin^2 2\theta = 2.5 \times 10^{-15}$ (note that errors are not quoted due to the inability of XSPEC to compute formal uncertainties on a small flux within the region of interest).

Furthermore, we estimated a 3σ upper limit of an undetected emission line at $\simeq$3.5 keV to be $F_{\rm DM} = 2.41 \times 10^{-6}$ photons cm^{-2} s^{-1}. The resulting maximum mixing angle from our 114 clusters is then $\sin^2(2\theta) = 4.4 \times 10^{-11}$, lower than the previous estimates for favoured mixing angles from cluster studies. These include the *XMM*-PN value for 73 clusters in B14 ($\sin^2(2\theta) \simeq 7 \times 10^{-11}$) and Bulbul et al. (2016) study of *Suzaku* observations for 47 clusters ($\sin^2(2\theta) \simeq 6 \times 10^{-11}$). Moreover, our result is comparable to among the most stringent constraints on the non-detection of a dark matter decay feature using *XMM* observations of Draco ($\sin^2(2\theta) \simeq 2 \times 10^{-11}$, Jeltema & Profumo 2016) and *XMM* blank sky observations (Dessert et al. 2020). Relevant constraints from previous studies are summarized in Fig. 8.

We conclude that although there is a measurable flux excess at $\simeq$3.5 keV in some cluster spectra (e.g. XCS J0003.3+0204), this is not a ubiquitous feature and hence unlikely to originate from sterile neutrino dark matter decay. We have carried out a series of checks to demonstrate that our methodology is not artificially masking the existence of a weak dark matter decay feature. We perform tests on our blueshifting technique to ensure that the purported 3.5-keV feature appears at the correct rest-frame energy, in addition to alternative weighting methods, abundance and photoelectric absorption models, and comparisons with spectroscopic data. We have found our methodology to be robust to these tests and have negligible impact on our presented results.

Future work on the constraining the origin of the purported 3.5-keV feature will be informed most directly by the launch of the *XRISM* satellite (the successor to the short-lived *Hitomi* mission). With significantly improved spectral resolution, it will be possible to determine the precise energies of elemental and unknown lines to clarify whether a $\simeq$3.5-keV flux excess is indeed originating from a discrete emission line (such as in the case of XCS J0003.3+0204). Moreover, deeper observations of single clusters with claimed $\simeq$3.5-keV emission such as Perseus will be able to confirm whether such a line exists, and if so, to what extent it is resolvable from the nearby K and Ar transition lines.

We further aim to revisit previous analyses such as B14, in which the cluster sample is produced using publicly available *XMM* observations. Given the complications associated with stacking methods and the fact that individual systems can contribute significantly to the appearance of a line in joint cluster searches, we will repeat the analysis in B14 simply by jointly fitting all available clusters in parallel, in addition to fitting each cluster individually. The aim of this would be to see if a $\simeq$3.5-keV excess is detected in any individual clusters in the B14 analysis, which could suggest that these clusters are responsible for an overall so-called dark matter decay feature (or masking one).

Given that two of the three clusters in this study with a measured flux excess at $\simeq$3.5 keV also display high rates of flaring, investigating the rate of flaring across all clusters which might contain such flux excesses would be a useful diagnostic to examine whether the origin of the line is instrumental. Deeper, repeated observations of individual clusters are also needed to further test the possibility of a variable $\simeq$3.5-keV feature (e.g. there is a hint of variability in the feature observed in XCS J1416.7+2315), which could lend support to the interpretation that $\simeq$3.5-keV emission arises from AGN variability (or the interaction between AGN and ALPs in a more exotic dark matter scenario).

Finally, further work to conclusively determine the existence and properties of the intriguing 3.5-keV feature will require even larger jointly fitted cluster samples. Hence, future work on this topic will involve a repeat of this analysis on a larger sample of redMaPPer selected clusters in the Dark Energy Survey Year 3 footprint with associated archival X-ray data.

ACKNOWLEDGEMENTS

The authors thank K. Abazajian for helpful discussions. S. B. is grateful to F. Hofmann for advice on X-ray analysis, S. Profumo for comments, and A. R. McDaniel for guidance with calculations. The authors would also like to thank the referee for useful suggestions. S. B., K. R., and P. G. acknowledge support from the UK Science and Technology Facilities Council via grants ST/N504452/1 (S. B.), ST/P000525/1 (K. R., P. G.). T. J. was supported by the National Science Foundation under grant no. 1517545. M. H. acknowledges financial support from the National Research Foundation and the University of KwaZulu-Natal. P. T. P. V. was supported by Fundação para a Ciência e a Tecnologia (FCT) through research grants UIDB/04434/2020 and UIDP/04434/2020. This research made use of ASTROPY,[4] a community-developed core PYTHON package for astronomy (Astropy Collaboration 2013, 2018), as well as NUMPY, SCIPY, and MATPLOTLIB. The data underlying this article are available in the article and in its online supplementary material.

REFERENCES

Abazajian K., Fuller G. M., Patel M., 2001, Phys. Rev. D, 64, 023501
Abell G. O., 1958, ApJS, 3, 211
Aharonian F. A. et al., 2017, ApJ, 837, L15
Aharonian Hitomi Collaboration F., 2018, PASJ, 70, 12
Anders E., Grevesse N., 1989, Geochim. Cosmochim. Acta, 53, 197
Anderson M. E., Churazov E., Bregman J. N., 2015, MNRAS, 452, 3905
Arnaud K. A., 1996, in Jacoby G. H., Barnes J., eds, ASP Conf. Ser. Vol. 101, Astronomical Data Analysis Software and Systems V. Astron. Soc. Pac., San Francisco, p. 17
Arnaud M., Pointecouteau E., Pratt G. W., 2005, A&A, 441, 893
Asplund M., Grevesse N., Sauval A. J., Scott P., 2009, ARA&A, 47, 481
Astropy Collaboration, 2013, A&A, 558, A33
Astropy Collaboration, 2018, AJ, 156, 123
Ben Bekhti N. et al., 2016, A&A, 594, A116

[4]http://www.astropy.org

Berg M., Conlon J. P., Day F., Jennings N., Krippendorf S., Powell A. J., Rummel M., 2017, ApJ, 847, 101
Böhringer H. et al., 2007, A&A, 469, 363
Böhringer H. et al., 2010, A&A, 514, A32
Böhringer H., Werner N., 2010, A&AR, 18, 127
Boyarsky A., Ruchayskiy O., Shaposhnikov M., 2009, Annu. Rev. Nucl. Part. Sci., 59, 191
Boyarsky A., Ruchayskiy O., Iakubovskyi D., Franse J., 2014, Phys. Rev. Lett., 113, 251301
Boyarsky A., Iakubovskyi D., Ruchayskiy O., Savchenko D., 2018, preprint (arXiv:1812.10488)
Bulbul E., Markevitch M., Foster A., Smith R. K., Loewenstein M., Randall S. W., 2014, ApJ, 789, 13 (B14)
Bulbul E., Markevitch M., Foster A., Miller E., Bautz M., Loewenstein M., Randall S. W., Smith R. K., 2016, ApJ, 831, 55
Cash W., 1979, ApJ, 228, 939
Dessert C., Rodd N. L., Safdi B. R., 2020, Science, 367, 1465
Ebeling H., Edge A. C., Allen S. W., Crawford C. S., Fabian A. C., Huchra J. P., 2000, MNRAS, 318, 333
Ettori S., Baldi A., Balestra I., Gastaldello F., Molendi S., Tozzi P., 2015, A&A, 578, A46
Foster A. R., Ji L., Smith R. K., Brickhouse N. S., 2012, ApJ, 756, 128
Franse J. et al., 2016, ApJ, 829, 124
Grevesse N., Sauval A. J., 1998, Space Sci. Rev., 85, 161
Gu L., Kaastra J., Raassen A. J. J., Mullen P. D., Cumbee R. S., Lyons D., Stancil P. C., 2015, A&A, 584, L11
Hofmann F., Wegg C., 2019, A&A, 625, L7
Holland J. G., Böhringer H., Chon G., Pierini D., 2015, MNRAS, 448, 2644
Jeltema T., Profumo S., 2015, MNRAS, 450, 2143
Jeltema T., Profumo S., 2016, MNRAS, 458, 3592
Kravtsov A. V., Borgani S., 2012, ARA&A, 50, 353
Lodders K., Palme H., Gail H.-P., 2009, Landolt Börnstein. p. 712
Łokas E. L., Mamon G. A., 2001, MNRAS, 321, 155
Lovisari L., Reiprich T. H., 2018, MNRAS, 483, 540
Malyshev D., Neronov A., Eckert D., 2014, Phys. Rev. D, 90, 103506
Maurogordato S., Sauvageot J. L., Bourdin H., Cappi A., Benoist C., Ferrari C., Mars G., Houairi K., 2011, A&A, 525, A79
Mernier F. et al., 2020, Astron. Nachr., 341, 203
Miraghaei H., Khosroshahi H. G., Sengupta C., Raychaudhury S., Jetha N. N., Abbassi S., 2015, AJ, 150, 196
Mohr J. J., Geller M. J., Wegner G., 1996, AJ, 112, 1816
Nulsen P. E. J., Fabian A. C., Mushotzky R. F., Boldt E. A., Holt S. S., Marshall F. J., Serlemitsos P. J., 1979, MNRAS, 189, 183
Pal P. B., Wolfenstein L., 1982, Phys. Rev. D, 25, 766
Riemer-Sørensen S., 2016, A&A, 590, A71
Romer A. K. et al., 2000, ApJS, 126, 209
Romer A. K., Viana P. T. P., Liddle A. R., Mann R. G., 2001, ApJ, 547, 594
Ruchayskiy O. et al., 2016, MNRAS, 460, 1390
Rykoff E. S. et al., 2014, ApJ, 785, 104
Shah C., Dobrodey S., Bernitt S., Steinbrügge R., Crespo López-Urrutia J. R., Gu L., Kaastra J., 2016, ApJ, 833, 52
Struble M. F., Rood H. J., 1987, ApJS, 63, 543
Tamura T. et al., 2019, PASJ, 71, 50
Tremaine S., Gunn J. E., 1979, Phys. Rev. Lett., 42, 407
Urban O., Werner N., Allen S. W., Simionescu A., Kaastra J. S., Strigari L. E., 2015, MNRAS, 451, 2447
Vikhlinin A., Kravtsov A., Forman W., Jones C., Markevitch M., Murray S. S., Van Speybroeck L., 2006, ApJ, 640, 691
Wilms J., Lee J. C., Nowak M. A., Schulz N. S., Xiang J., Juett A., 2010, in AAS/High Energy Astrophysics Division #11. p. 674

APPENDIX A: FULL DATA SAMPLE

Table A1 provides the X-ray properties and associated projected dark matter masses for the 117 clusters used in this study.

Table A1. Properties of the cluster sample. XCSIDS with an ∗ denote clusters that were part of the B14 analysis.

XCSID	$z_{\rm phot}^{\rm RM}$	$T_{\rm X}$ (keV)	$M_{\rm DM}^{\rm proj}$ ($10^{14}M_{\odot}$)	ObsID	$n_{\rm H}$ ($\rm cm^{-2}$)
XMMXCSJ000312.1–060530.5	0.251	$6.81^{+0.22}_{-0.13}$	6.52	0652010401	0.012
XMMXCSJ000349.3+020404.8	0.11	$4.78^{+0.12}_{-0.12}$	3.8	0201900101	0.01
XMMXCSJ001053.4+290939.6	0.338	$4.93^{+0.38}_{-0.37}$	3.59	0650380101	0.024
XMMXCSJ001737.5–005234.2	0.219	$4.1^{+0.22}_{-0.22}$	2.78	0403760701	0.022
XMMXCSJ001833.2+162609.9	0.562	$9.66^{+0.37}_{-0.36}$	10.03	0111000101	0.021
XMMXCSJ001938.0+033635.3	0.273	$6.26^{+0.15}_{-0.15}$	5.59	0693010301	0.035
XMMXCSJ002635.9+170930.7	0.394	$3.43^{+0.19}_{-0.14}$	1.87	0050140201	0.03
XMMXCSJ003456.6+023357.9	0.379	$5.53^{+0.53}_{-0.41}$	4.27	0650380601	0.017
XMMXCSJ003706.4+090925.8	0.264	$8.24^{+0.26}_{-0.26}$	8.98	0084230201	0.049
XMMXCSJ004630.7+202803.6	0.105	$2.44^{+0.23}_{-0.23}$	1.21	0652460101	0.031
XMMXCSJ005138.5+271958.8	0.38	$6.83^{+0.42}_{-0.32}$	6.13	0650380701	0.02
XMMXCSJ005559.1+261949.0	0.196	$5.84^{+0.16}_{-0.16}$	5.15	0203220101	0.028
XMMXCSJ010649.3+010324.7	0.25	$2.89^{+0.04}_{-0.04}$	1.51	0762870601	0.036
XMMXCSJ013724.6–082727.6	0.557	$7.87^{+0.67}_{-0.66}$	7.08	0700180201	0.01
XMMXCSJ014656.7–092940.5	0.429	$5.09^{+0.36}_{-0.35}$	3.6	0673750101	0.029
XMMXCSJ015242.1+010029.4	0.231	$5.38^{+0.31}_{-0.15}$	4.4	0084230401	0.029
XMMXCSJ015334.1–011816.1	0.245	$5.05^{+0.19}_{-0.19}$	3.93	0762870401	0.029
XMMXCSJ015707.7–055233.7	0.132	$4.09^{+0.24}_{-0.23}$	2.89	0781200101	0.032
XMMXCSJ015824.9–014654.3	0.157	$2.74^{+0.11}_{-0.11}$	1.44	0762870301	0.008
XMMXCSJ020143.0–021146.5	0.198	$3.55^{+0.08}_{-0.08}$	2.19	0605000301	0.022
XMMXCSJ021441.2–043313.8	0.143	$5.25^{+0.25}_{-0.22}$	4.4	0553911401	0.02

Table A1 – *continued*

XCSID	$z_{\rm phot}^{\rm RM}$	$T_{\rm X}$ (keV)	$M_{\rm DM}^{\rm proj}$ ($10^{14}M_{\odot}$)	ObsID	$n_{\rm H}$ ($\rm cm^{-2}$)
XMMXCSJ022145.6–034613.7	0.422	$4.84^{+0.41}_{-0.41}$	3.33	0604280101	0.009
XMMXCSJ023142.5–045254.5	0.194	$4.41^{+0.17}_{-0.18}$	3.19	0762870201	0.023
XMMXCSJ023953.0–013441.1	0.358	$5.91^{+0.16}_{-0.16}$	4.84	0782150101	0.043
XMMXCSJ024803.3–033143.4∗	0.195	$3.78^{+0.06}_{-0.06}$	2.45	0084230501	0.011
XMMXCSJ024811.9–021624.9	0.241	$7.74^{+0.36}_{-0.36}$	8.15	0721890401	0.033
XMMXCSJ025632.9+000558.5	0.364	$4.9^{+0.12}_{-0.12}$	3.51	0801610101	0.016
XMMXCSJ073220.2+313751.1	0.182	$5.94^{+0.16}_{-0.16}$	5.34	0673850201	0.017
XMMXCSJ080056.7+360323.0	0.292	$5.93^{+0.21}_{-0.21}$	5.03	0781590201	0.017
XMMXCSJ082318.4+155758.0	0.159	$3.01^{+0.2}_{-0.19}$	1.69	0742510401	0.029
XMMXCSJ082557.4+041445.6	0.238	$4.65^{+0.28}_{-0.27}$	3.42	0762950301	0.049
XMMXCSJ085026.7+001506.2	0.201	$3.21^{+0.18}_{-0.18}$	1.84	0761730501	0.051
XMMXCSJ085612.8+375605.7	0.401	$5.42^{+0.52}_{-0.31}$	4.08	0302581801	0.014
XMMXCSJ090036.8+205340.6	0.244	$3.91^{+0.09}_{-0.09}$	2.54	0402250701	0.03
XMMXCSJ090849.1+143831.6	0.442	$3.34^{+0.21}_{-0.17}$	1.74	0674370201	0.048
XMMXCSJ090851.4+144550.0	0.457	$5.32^{+0.45}_{-0.42}$	3.84	0674370201	0.037
XMMXCSJ090912.4+105831.2	0.176	$5.38^{+0.26}_{-0.16}$	4.52	0673850901	0.017
XMMXCSJ091048.8+385007.5	0.564	$9.55^{+0.78}_{-0.78}$	9.81	0723780101	0.032
XMMXCSJ091110.7+174627.4	0.514	$6.61^{+0.33}_{-0.3}$	5.38	0693662501	0.019
XMMXCSJ091345.5+405626.3	0.424	$5.94^{+0.25}_{-0.25}$	4.71	0147671001	0.02
XMMXCSJ091752.2+514332.6∗	0.228	$7.25^{+0.2}_{-0.2}$	7.35	0084230601	0.008
XMMXCSJ092018.6+370622.2	0.239	$2.63^{+0.05}_{-0.05}$	1.29	0149010201	0.014
XMMXCSJ094300.0+465937.3	0.348	$5.09^{+0.18}_{-0.18}$	3.77	0106460101	0.045
XMMXCSJ100304.6+325339.3	0.391	$3.17^{+0.26}_{-0.26}$	1.64	0302581601	0.03
XMMXCSJ100742.4+380046.1	0.106	$3.24^{+0.16}_{-0.16}$	1.96	0653450201	0.013
XMMXCSJ101703.4+390250.1	0.208	$6.11^{+0.13}_{-0.13}$	5.54	0084230701	0.023
XMMXCSJ102339.7+041115.3∗	0.291	$5.4^{+0.03}_{-0.03}$	4.3	0605540201	0.021
XMMXCSJ103801.2+414619.8	0.133	$2.07^{+0.21}_{-0.15}$	0.9	0206180101	0.016
XMMXCSJ104044.2+395711.1∗	0.142	$3.79^{+0.05}_{-0.05}$	2.52	0147630101	0.019
XMMXCSJ104545.6+042025.4	0.15	$2.87^{+0.25}_{-0.21}$	1.57	0653450601	0.034
XMMXCSJ104724.0+151436.0	0.214	$3.82^{+0.3}_{-0.3}$	2.47	0721880101	0.007
XMMXCSJ111253.4+132640.2∗	0.181	$4.78^{+0.08}_{-0.08}$	3.68	0500760101	0.035
XMMXCSJ113313.2+500838.5	0.367	$4.73^{+0.33}_{-0.33}$	3.29	0650382001	0.021
XMMXCSJ114224.9+583134.7	0.326	$7.75^{+0.75}_{-0.75}$	7.82	0650382201	0.022
XMMXCSJ114935.6+222401.8	0.529	$8.55^{+0.76}_{-0.55}$	8.29	0693661701	0.018
XMMXCSJ115518.2+232424.3	0.135	$6.31^{+0.07}_{-0.07}$	6.06	0551280201	0.024
XMMXCSJ115827.8+262943.4	0.141	$1.68^{+0.2}_{-0.05}$	0.63	0601260201	0.014
XMMXCSJ120022.7+032007.4	0.138	$5.94^{+0.12}_{-0.12}$	5.45	0827010301	0.006
XMMXCSJ121937.0–031840.9	0.295	$4.75^{+0.35}_{-0.35}$	3.45	0693010401	0.015
XMMXCSJ122656.3+334332.8	0.514	$4.73^{+0.33}_{-0.32}$	3.04	0200340101	0.022
XMMXCSJ123355.5+152608.2	0.23	$5.19^{+0.23}_{-0.23}$	4.15	0404120101	0.029
XMMXCSJ123422.8+094718.7	0.239	$4.26^{+0.16}_{-0.1}$	2.94	0673851101	0.024
XMMXCSJ123618.1+285901.9	0.222	$3.33^{+0.35}_{-0.23}$	1.94	0722660201	0.067
XMMXCSJ123658.8+631117.9	0.3	$6.43^{+0.45}_{-0.43}$	5.77	0402250101	0.04
XMMXCSJ124133.3+325023.7	0.352	$5.56^{+0.47}_{-0.39}$	4.37	0056020901	0.034
XMMXCSJ124401.5+165347.3	0.542	$4.2^{+0.22}_{-0.17}$	2.44	0302581501	0.021
XMMXCSJ130357.9+673055.2	0.222	$3.8^{+0.26}_{-0.26}$	2.43	0136000101	0.015
XMMXCSJ130749.5+292549.3	0.261	$3.11^{+0.18}_{-0.18}$	1.7	0205910101	0.048
XMMXCSJ131129.8–012024.5∗	0.185	$8.06^{+0.08}_{-0.08}$	8.99	0093030101	0.018
XMMXCSJ131145.1+220206.1	0.17	$3.52^{+0.32}_{-0.27}$	2.2	0402250301	0.046

Table A1 – *continued*

XCSID	$z_{\rm phot}^{\rm RM}$	$T_{\rm X}$ (keV)	$M_{\rm DM}^{\rm proj}$ ($10^{14}M_{\odot}$)	ObsID	$n_{\rm H}$ ($\rm cm^{-2}$)
XMMXCSJ132250.7+313911.4	0.317	$6.65^{+0.55}_{-0.32}$	6.05	0650384601	0.012
XMMXCSJ133048.5–015149.4	0.103	$4.21^{+0.07}_{-0.07}$	3.08	0112240301	0.018
XMMXCSJ133108.4–014338.4	0.545	$3.79^{+0.25}_{-0.25}$	2.04	0112240301	0.024
XMMXCSJ133233.8+502450.2	0.274	$5.94^{+0.35}_{-0.35}$	5.1	0142860201	0.039
XMMXCSJ133244.2+503243.5	0.286	$7.24^{+0.22}_{-0.23}$	7.11	0142860201	0.01
XMMXCSJ133421.5+503058.9	0.585	$4.62^{+0.39}_{-0.38}$	2.8	0111160101	0.026
XMMXCSJ133519.5+410004.9∗	0.234	$7.16^{+0.25}_{-0.25}$	7.16	0084230901	0.015
XMMXCSJ133648.8+102624.0	0.159	$3.1^{+0.22}_{-0.22}$	1.78	0761590701	0.034
XMMXCSJ140101.9+025238.3∗	0.253	$6.52^{+0.04}_{-0.04}$	6.04	0551830201	0.036
XMMXCSJ141627.7+231523.5	0.137	$3.28^{+0.12}_{-0.12}$	1.98	0722140401	0.019
XMMXCSJ141956.1+063434.9	0.541	$4.23^{+0.43}_{-0.36}$	2.47	0303670101	0.021
XMMXCSJ142039.8+395505.8	0.575	$8.1^{+0.48}_{-0.48}$	7.36	0693661001	0.018
XMMXCSJ142348.0+240444.1	0.523	$5.63^{+0.16}_{-0.16}$	4.08	0720700301	0.018
XMMXCSJ142521.4+631143.1	0.14	$4.86^{+0.13}_{-0.13}$	3.87	0765031201	0.049
XMMXCSJ142601.0+374937.0∗	0.175	$8.3^{+0.11}_{-0.11}$	9.5	0112230201	0.018
XMMXCSJ143150.0+133159.5	0.166	$3.63^{+0.16}_{-0.16}$	2.32	0601970101	0.033
XMMXCSJ144219.8+221809.9	0.107	$3.49^{+0.11}_{-0.16}$	2.23	0765010501	0.015
XMMXCSJ145715.0+222032.3	0.267	$4.47^{+0.06}_{-0.06}$	3.15	0108670201	0.036
XMMXCSJ150019.6+212214.5	0.162	$5.78^{+0.15}_{-0.15}$	5.15	0693011001	0.023
XMMXCSJ150817.8+575437.8	0.55	$8.36^{+0.72}_{-0.54}$	7.88	0723780501	0.023
XMMXCSJ151012.0+333058.0∗	0.121	$6.34^{+0.15}_{-0.15}$	6.14	0149880101	0.025
XMMXCSJ151618.5+000532.4	0.12	$4.69^{+0.09}_{-0.09}$	3.66	0201902001	0.021
XMMXCSJ151820.6+292735.3	0.558	$6.45^{+0.25}_{-0.25}$	5.04	0693661101	0.023
XMMXCSJ152642.6+164734.9	0.341	$4.47^{+0.28}_{-0.27}$	3.03	0650382801	0.018
XMMXCSJ152925.0+104144.0	0.488	$5.01^{+0.16}_{-0.16}$	3.4	0762520201	0.019
XMMXCSJ153253.8+302100.5∗	0.357	$5.03^{+0.08}_{-0.08}$	3.67	0651240101	0.008
XMMXCSJ153941.0+342512.8	0.236	$6.7^{+0.28}_{-0.27}$	6.39	0673850601	0.046
XMMXCSJ163936.8+470310.0	0.226	$4.04^{+0.36}_{-0.33}$	2.7	0761590401	0.032
XMMXCSJ164020.2+464227.1	0.233	$9.86^{+0.3}_{-0.3}$	12.39	0605000501	0.023
XMMXCSJ165943.9+323654.9	0.102	$3.71^{+0.3}_{-0.31}$	2.48	0083150801	0.012
XMMXCSJ172227.0+320758.0	0.229	$7.09^{+0.14}_{-0.14}$	7.06	0693180901	0.019
XMMXCSJ212939.7+000516.9∗	0.248	$5.2^{+0.06}_{-0.06}$	4.12	0093030201	0.033
XMMXCSJ213516.8+012600.0	0.237	$8.59^{+0.58}_{-0.32}$	9.76	0692931301	0.017
XMMXCSJ215101.0–073633.5	0.274	$4.13^{+0.12}_{-0.12}$	2.74	0744390301	0.021
XMMXCSJ215337.0+174146.9∗	0.251	$10.08^{+0.25}_{-0.25}$	12.75	0111270101	0.02
XMMXCSJ221145.8–034936.8	0.424	$10.55^{+0.24}_{-0.24}$	12.59	0693010601	0.016
XMMXCSJ222353.0–013714.4	0.101	$4.39^{+0.08}_{-0.1}$	3.31	0401920101	0.016
XMMXCSJ222605.0+172220.2	0.114	$6.17^{+0.08}_{-0.08}$	5.88	0762470101	0.038
XMMXCSJ222831.6+203729.9	0.413	$8.09^{+0.26}_{-0.26}$	8.04	0147890101	0.044
XMMXCSJ224321.4–093550.2	0.435	$6.77^{+0.17}_{-0.09}$	5.86	0503490201	0.015
XMMXCSJ224413.0–093427.9	0.444	$3.45^{+0.33}_{-0.24}$	1.84	0503490201	0.04
XMMXCSJ224523.7+280802.8	0.346	$5.63^{+0.52}_{-0.51}$	4.48	0650384401	0.05
XMMXCSJ230821.8–021127.4	0.3	$7.81^{+0.49}_{-0.49}$	8.04	0205330501	0.021
XMMXCSJ231132.6+033759.9	0.304	$6.55^{+0.27}_{-0.27}$	5.93	0693010101	0.044
XMMXCSJ231825.4+184246.9	0.163	$3.33^{+0.11}_{-0.11}$	2.0	0762950201	0.039
XMMXCSJ233738.6+001614.5	0.295	$7.21^{+0.36}_{-0.36}$	7.02	0042341301	0.02
XMMXCSJ234116.6–090128.8	0.258	$6.77^{+0.35}_{-0.24}$	6.43	0693010801	0.023

APPENDIX B: MOS DATA FOR INDIVIDUAL CLUSTERS

Fig. B1 shows the corresponding trends in ΔC for the three individual clusters in the analysis using available MOS data.

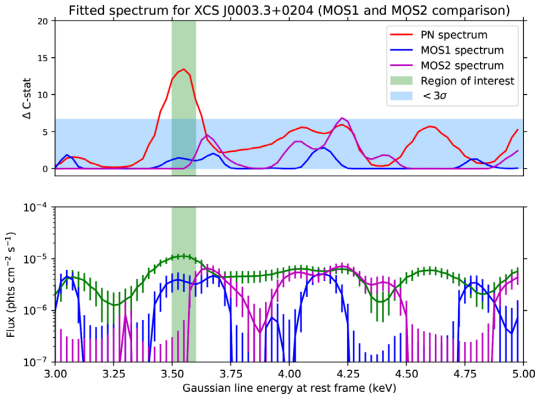

(a)

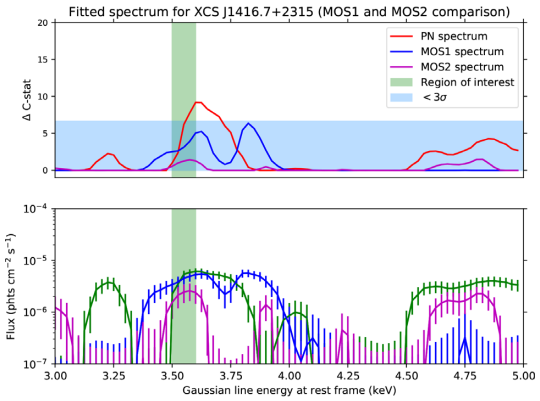

(b)

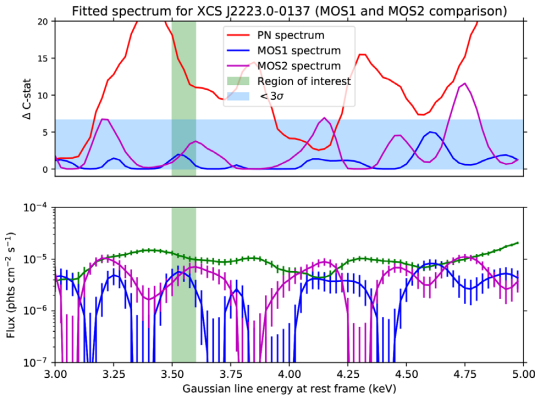

(c)

Figure B1. Comparisons in the trend of ΔC for (a) XCS J0003.3+0204, (b) XCSJ1416.7+2315, and (c) XCS J2223.0–0137 using the highest quality PN and MOS observation for each cluster (described in Section 5.1). In the top panels, the ΔC trend is displayed for the PN (red), MOS1 (blue), and MOS2 (magenta) spectra. In the bottom panels, the corresponding Gaussian normalization and associated error bars are shown.

APPENDIX C: SPECTROSCOPIC REDSHIFT COMPARISONS

Fig. C1 shows the comparison in the ΔC trend for two clusters using available spectroscopic data.

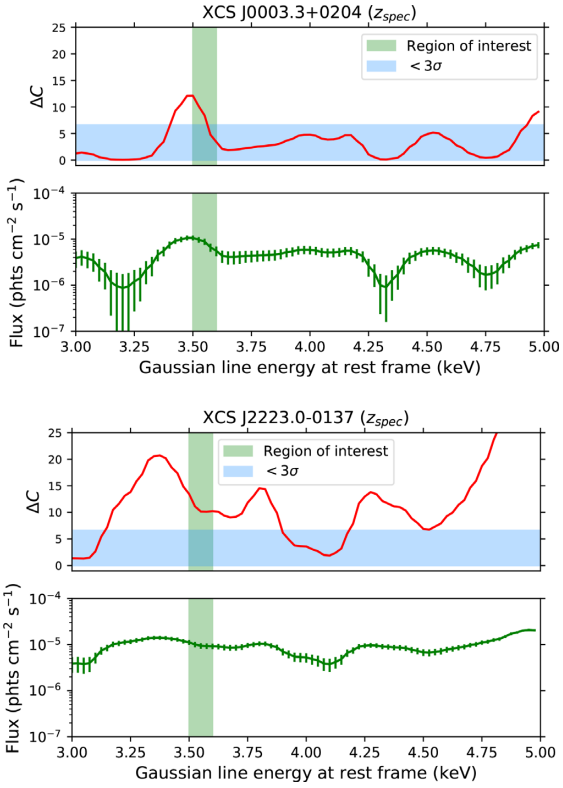

Figure C1. Comparisons in the trend of ΔC for XCS J0003.3+0204 (top) and XCS J2223.0–0137 (bottom) when replacing the RM photometric estimated redshift with available spectroscopic redshifts (see Section 5.2.5).

This paper has been typeset from a TEX/LATEX file prepared by the author.